Robust Near-Wall Skin-Friction Evaluation from PIV

Drag reduction across an oscillating wall

Nicolò Scaiola

TU Delft

Politecnico di Torino

Politecnico di Torino - Department of Mechanical and Aerospace Engineering

Master of Science Thesis

Robust Near-Wall Skin-Friction Evaluation from PIV

Drag reduction across an oscillating wall

CANDIDATE:	SUPERVISORS:	
Nicolò SCAIOLA s323256	Prof.	Gioacchino CAFIERO
	Dir. Ir.	Ferry SCHRIJER
	Prof. Dr.	Fulvio SCARANO
	MSc	Marco GALLI

Academic year 2025-2026

Abstract

Skin-friction drag accounts for approximately 50% of the total aerodynamic drag experienced by a commercial aircraft in cruise; this motivates the development of flow control strategies and accurate measurement techniques capable of resolving small variations in wall-shear stress. In the present thesis, the spatial evolution of a turbulent boundary layer at $Re_\tau \approx 470$ developing across a finite spanwise oscillating wall is experimentally investigated; the non-dimensional actuation parameters set to $T^+ \approx 100$ and $W_m^+ \approx 7$, correspond to a measured skin-friction reduction of approximately 30%.

The spatial distribution of skin friction is obtained by adopting a recently introduced near-wall data regression method based on a non-linear arctangent fit, which allows for the use of data up to $y^+ \approx 15$ circumventing the need of high spatial resolution for the PIV measurements. The performance of the method is assessed with synthetic data, and the trends are cross validated through the analysis of the experimental data.

The skin-friction coefficient response is observed to follow a simple exponential law for both the adaptation and recovery transients with a characteristic length scale of approximately one boundary layer thickness δ. Surprisingly, the latter is found to persist over a length comparable to that of the adaptation transient, in contrast with previous reports of a faster recovery.

Table of Contents

Figures

Tables

Nomenclature

Roman Symbols

A_{osc}	Peak-to-peak amplitude of the wall oscillation	$[m]$
B	Additive constant of the logarithmic law (≈ 5.0)	$[-]$
C_f	Skin friction coefficient	$[-]$
D	Drag force	$[N]$
d_p	Particle diameter (seeding)	$[m]$
f	Frequency	$[Hz]$
$f_\#$	F-stop (aperture setting of the camera)	$[-]$
h	Window size (wall normal)	$[m]$
H	Shaper factor	$[-]$
L	Oscillating plate lenght	$[m]$
M	Magnification factor	$[-]$
P	Power	$[W]$
Re_x	Reynolds number ($u_\infty x/\nu$)	$[-]$
Re_τ	Friction Reynolds number ($u_\tau \delta/\nu$)	$[-]$
Re_θ	Momentum thickness Reynolds number ($u_\tau \theta/\nu$)	$[-]$
$\mathcal{R}$ (DR)	Drag Reduction	$[\%]$
S	Wetted surface	$[m^2]$
St	Stokes number	$[-]$
T	Period of oscillation	$[s]$
u_τ	Friction velocity $\left(\sqrt{\tau_w/\rho}\right)$	$[m/s]$
U_∞	Free-stream velocity	$[m/s]$
W_m	Maximum spanwise velocity of the oscillating wall	$[m/s]$
x, y, z	Streamwise, wall-normal, and spanwise coordinates	$[m]$

Acronyms

CCD	Charge-Coupled Device
CMOS	Complementary Metal-Oxide Semiconductor
CO_2	Carbon dioxide
DOF	Degree of freedom
DNS	Direct Numerical Simulation
DR	Drag Reduction
FOV	Field of View
IW	Interrogation Window
LBL	Laminar Boundary Layer
LE	Leading Edge
LSS	Low Speed Streaks
NWC	Near-Wall Cycle
PIV	Particle Image Velocimetry
PTV	Particle Tracking Velocimetry
QSV	Quasi-Streamwise Vortices
SNR	Signal to Noise Ratio
TE	Trailing Edge
TBL	Turbulent Boundary Layer
TRL	Technology Readiness Level
ZPG	Zero Pressure Gradient

Greek Symbols

Δt	Time separation between laser pulses	$[s]$
δ	Boundary layer thickness (usually δ^{99})	$[m]$
δ^*	Displacement Thickness	$[m]$
δ_v	Viscous length scale	$[m]$
δ_z	Stokes' layer thickness	$[m]$
θ	Momentum thickness	$[m]$
κ	Von Kármán constant (≈ 0.41)	$[-]$
μ	Dynamic viscosity	$[Kg/(m \cdot s)]$
ν	Cinematic viscosity	$[m^2/s]$
ξ	Spatial transients length scale	$[m]$
τ_p	Particle relaxation time	$[s]$
τ_w	Wall shear stress	$[Pa]$
ω	Angular frequency (2πf)	$[rad/s]$

Notation

$(\cdot)^+$	Normalized by viscous units (u_τ, ν) of the reference case
$(\cdot)^*$	Normalized by viscous units (u_τ, ν) of the actual condition
$(\cdot)'$	Fluctuating component (Reynolds decomposition)
$(\cdot)_0$	Reference (uncontrolled) condition
$(\cdot)_c$	Controlled state
$(\cdot)_{rms}$	Root Mean Square
$(\cdot)_\infty$	Free-stream condition
$(\cdot)_w$	Value at the wall
$\bar{\cdot}$, $\langle\cdot\rangle$	Mean value

CHAPTER I

Context and Scientific Relevance

The following chapter establishes the industrial and scientific context motivating the present research, moving from a high-level introduction to the necessity of increased energy efficiency for the transport sector to the specific challenges in aerodynamic drag reduction and its measurement. The discussion briefly touches upon technical aspects introducing the research questions that will be detailed in subsequent chapters and concludes with an outline of the thesis structure.

1.1 Context and scientific relevance

In a world where energy efficiency is increasingly becoming a priority for all industrial sectors, commercial aviation is no exception, as power savings are pursued both from a purely economic standpoint and an environmental point of view. The transportation sector is a major contributor to global greenhouse gas emissions, with the aviation sector alone contributing about 2–3% of global anthropogenic CO_2 emissions [1]. Commercial aviation is particularly challenging to decarbonise due to strict safety, performance, and energy-density requirements. Nevertheless, significant progress has been made in improving overall energy efficiency; however, an increasing demand has led to the continued rise of the sector's environmental impact.

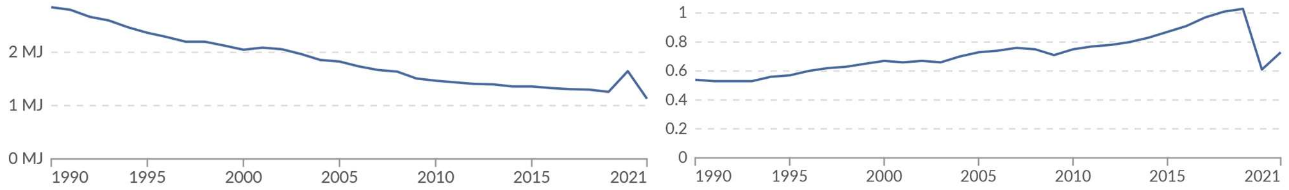

Figure 1 Left: energy intensity in the aviation sector $MJ/(Km \cdot pass)$*. Right:* CO_2 *emission of the aviation sector in billion tonnes [2].*

Over the past decades, the largest improvements in aircraft efficiency have been achieved through advancements in propulsion systems; however, further improvements are expected to be progressively more challenging and of diminishing returns due to both physical and practical constraint [3]. Alternative approaches such as sustainable aviation fuels, hybrid-electric propulsion, and hydrogen-powered aircraft are being actively investigated; these solutions, while promising significant results, still face challenges in terms of scalability and infrastructural needs [4]. At the same time, improvements in aerodynamic efficiency remain a key enabler for reducing fuel burn and emissions across all transportation sectors. For subsonic streamlined bodies, friction drag represents a significant portion of the total accounting for up to 50% of the drag experienced by an aircraft in cruising conditions [5]; even modest reductions can therefore lead to substantial fuel savings.

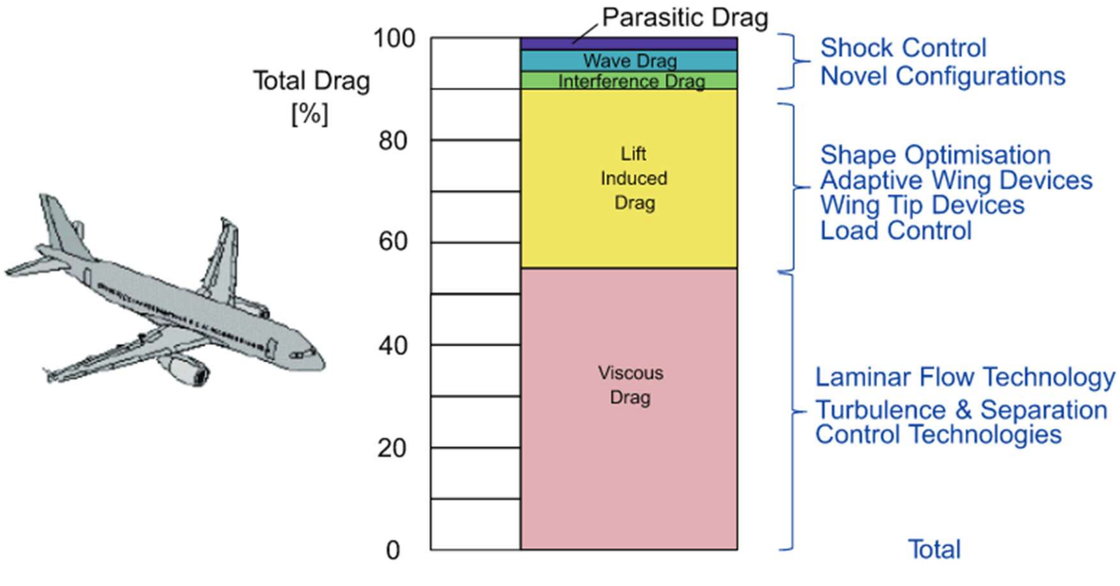

Figure 2 Schematics of Drag components for cruising aircraft and drag reduction potential analysis [5].

1.2 Prospects of Turbulent Drag Reduction research

While passive flow control technologies like riblets are industrially mature, active flow control has demonstrated the potential for skin-friction reductions exceeding 40% [6]. Additionally, despite the significant energetic penalties and low real world applicability associated with active systems, the study of said techniques provides an essential framework for understanding the physics of turbulence suppression.

Within this context the investigation of drag reduction via spanwise wall forcing is not to be taken in a vacuum but is foundational to the development of next-generation passive solutions reliant on the same physical mechanism. Sinusoidal or 'wavy' riblets [7] are already part of the scientific discourse and similar concepts based on discrete manipulation of the flow have recently been brought forward as well.

A major hurdle in reproducing the drag reduction mechanism with discrete passive manipulation lays in the complex spatial evolution of the flow when interacting with the control section. The adaptation to the flow control is not instantaneous and the drag reduction does not appear instantly nor it vanishes downstream; rather the flow possess a sort of spatial/temporal memory. It is clear that, being able to map the transient regions, is critical for the design of optimal design and placement of passive flow control technologies.

Precisely quantifying the spatial response still remains an open experimental challenge due to the significant experimental constraints. Standard non-intrusive techniques such as PIV stand out among the rest, but still they often struggle resolving the flow field close to the wall where the friction drag reduction is easily measured. Consequently this thesis focuses on closing this gap by developing and validating a robust skin friction evaluation methodology from PIV velocity data allowing for a precise evaluation of the skin friction coefficient evolution across the oscillating surface. The resulting evolution of the Drag reduction is then measured and modelled with a proposed exponential functional form.

1.3 Outline of the thesis

This research investigates skin-friction drag reduction through spanwise wall oscillation and develops experimental and data-analysis tools required for such investigations. The thesis is therefore structured to guide the reader from the fundamental physics of wall turbulence and active flow control to the need for a novel diagnostic tool, its introduction and validation. Finally, the method is applied for characterization of the spatial evolution of the skin friction coefficient in presence of the flow control.

Chapter two serves as a review of the relevant concepts and literature that will be referred to in the remainder of the thesis. The discussion covers the fundamentals of wall bounded flows and friction drag.

Chapter three introduces briefly the concept of turbulent drag reduction and the different flow control techniques available. Most of the chapter is dedicated to the description of spanwise wall forcing, the proposed physical mechanism, the actuation parameters and the spatial effects. This section closes addressing the research gap that this thesis is set to close.

Chapter four briefly introduces skin friction measurement techniques and focuses on the fundamental concepts and declinations of the measurement techniques of choice, Particle Image Velocimetry.

Chapter five discusses wall shear stress evaluation from PIV data introducing traditional techniques with their limitations as well as setting the ground for the use of novel non-linear methodologies.

Chapter six takes a deep dive on the validation of the proposed arctangent model against DNS data. In this section the method robustness and accuracy are compared to the classic linear fit. The analysis starts with the raw synthetic data and gradually introduces modelling of the artefacts typical of PIV experimental measurements and finally showing the accordance in the results obtained with real data.

Chapter seven describes the experimental setup in its entirety from the wind tunnel to the PIV system and parameters. Additionally, the data processing workflow is briefly discussed.

Chapter eight presents the results obtained, starting from the validation of the TBL tripping effectiveness to the streamwise evolution of the skin friction coefficient and its modelling.

Finally, a summary of the main results and recommendations for future work are given in Chapter nine.

CHAPTER II

Drag and Turbulent Boundary Layer

A good understanding of the base flow is a prerequisite to the study of any flow control technique aimed at turbulence suppression. This chapter serves as a review of the fundamental physics of wall bounded flows moving from the introduction of viscous drag to the statistical description of the canonical Turbulent Boundary Layer. Special attention is put on the coherent structures inhabiting the inner region of a TBL as their interaction stands as the motor of turbulence and their modulation underlies the drag reduction strategy of interest.

2.1 Friction Drag

By definition Drag is a force that resists the relative motion of a body wetted by a fluid. Depending on the case study aerodynamic drag can be divided in different component, but, on a fundamental level one can always identify two parts:

- Pressure Drag:
  Defined as the integral of the pressure (normal) forces over the body's surface, it is therefore related to the anisotropic pressure field that develops around said body.
- Viscous Drag:
  Defined as the integral of the shear (tangential) forces, it is related to the viscosity of the fluid and velocity gradients.

For streamlined bodies, when the relative speeds are limited to the subsonic regime, the Viscous Drag plays a major role, e.g. viscous drag accounts for ~ 60% of the total drag experienced by cruising airliners. To have a real world example one can cite the case of a trans-continental B747 where a 1% reduction in skin-friction drag would translate to a 0.75% fuel saving and a reduction of CO_2 production by 23 tonnes per flight [8].
A common way to evaluate skin friction drag is to make use of the skin friction coefficient of the object in the condition being studied. The skin friction coefficient C_f is a non-dimensional parameter characteristic of an object in a certain flow field from which one can quickly evaluate friction drag as follows:

$$D_f = \frac{1}{2} C_f \rho V_\infty^2 S$$

As previously mentioned, Viscous Drag is related with viscosity of the fluid; if interested in investigating said force, one should therefore look at region where viscous effects are significant. Traditional flows at high Reynolds numbers can be divided into two distinct regions. In the main body of the flow, called the outer region, viscosity can be neglected and the flow field is then obtained from an inviscid solution. However, closer to the wall, there is a very thin region called the boundary layer where viscous effects are important. The boundary layer is defined as a region of high shear where the velocity changes rapidly (in wall normal direction) to match that of the wall; this is due to continuous interactions between the fluid molecules and the solid surface, which give rise to the no-slip condition.

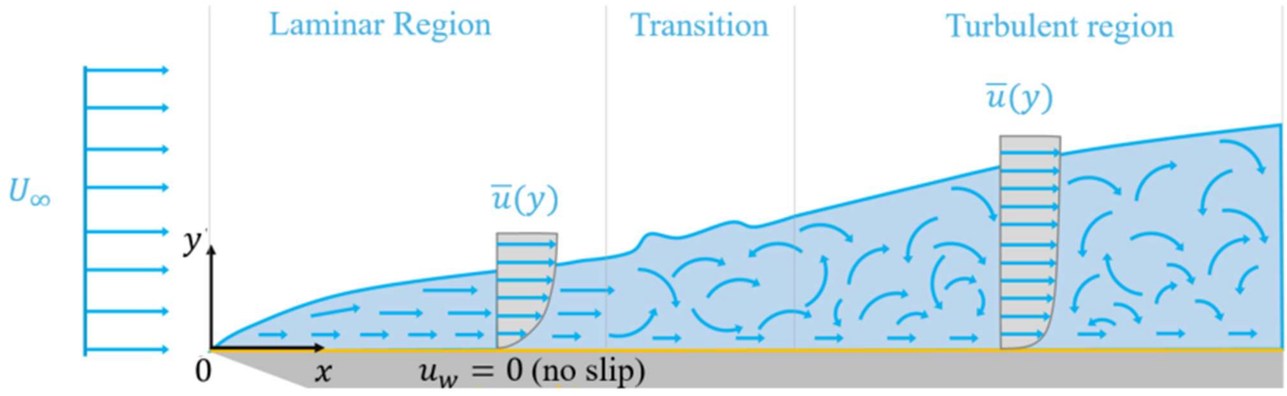

Figure 3 Schematics of Boundary layer. Adapted from [9].

This continued interaction causes the rise of a tangential stress at the wall [1] $\tau_w = \mu(du/dy)_w$acting in the same direction, but with opposite sense of relative motion; skin friction drag can be retrieved integrating said shear stress across the whole wetted surface.

A boundary layer can exist in two regimes depending on the Reynolds number associated to it:

- Laminar Boundary Layer:
  typical of 'low' Reynolds flows a LBL is characterized by an organized flow in which perturbations are quickly damped. This kind of boundary layer presents a relatively low velocity gradient at the wall and is therefore associated with lower skin friction.

- Turbulent Boundary Layer:
  typical of 'high' Reynolds flows, is significantly more complex and rich in 'structures. The interaction of the different structures causes high momentum diffusion sustaining higher velocity close to the wall and therefore causing higher viscous stresses.

Considering most of the transport sector is characterized by high velocity and/or significant length scale TBLs are ubiquitous.

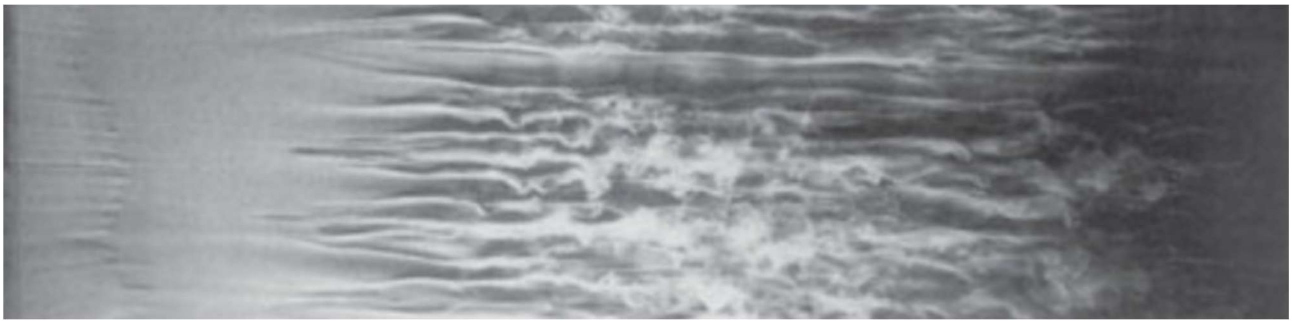

Figure 4 Top-down view of BL transition across a flat plate. Image from H. Werlé, ONERA, France.

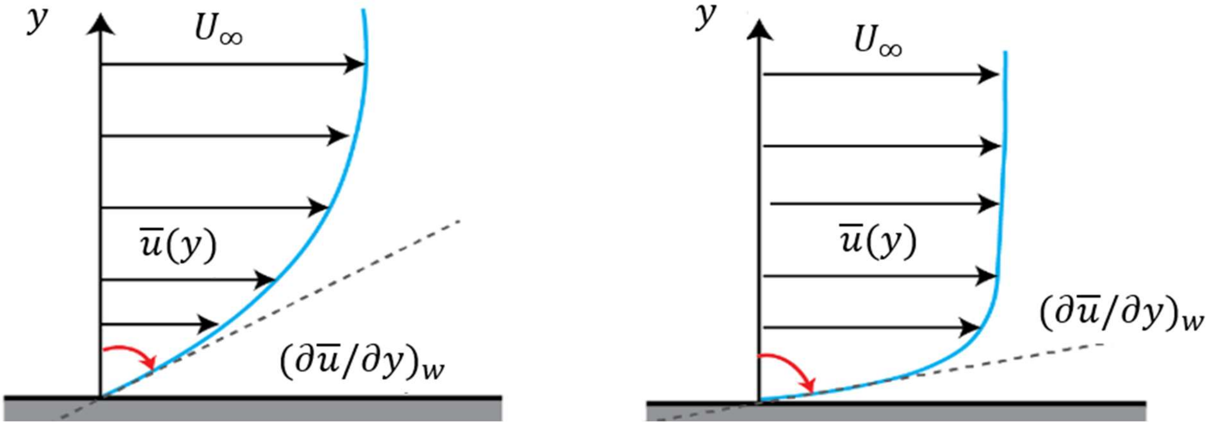

Figure 5 Mean streamwise velocity profile as a function of distance from the wall. Left: LBL. Right: TBL. Adapted from [10].

---

[1] The skin friction coefficient represents the non-dimensionalized version of the wall shear stress

2.2 Turbulent Boundary layer

To identify a viable control strategy, one must first understand the structure of the uncontrolled Turbulent Boundary Layer in a Zero Pressure Gradient condition. A TBL is not a random region in a strict sense, but it is simply a region highly sensitive to border and initial conditions; this sensitivity leads to complex velocity fields, but one can still infer statistical properties, recurring structures and events.

The standard framework for analysing turbulent flows involves the Reynolds decomposition, where the instantaneous field associated with each thermodynamic variable is defined as the sum of a time averaged mean component and a fluctuating part; sticking to the velocity field we get:

$$u_i(\vec{x},t) = \bar{u}_i(\vec{x}) + u_i'(\vec{x},t)$$

By definition, the mean of the fluctuations is zero, but the second order moments of these fluctuations, known as Reynolds stresses $\left(\rho \left\langle u_i' u_j' \right\rangle\right)$ do not vanish.

2.2.1 Statistical description of the canonical Turbulent Boundary Layer

The mean velocity profile in a fully developed TBL in a ZPG condition is characterized by a layered structure based on the distance from the wall. It can be divided in an outer region whose form is dependent on the external flow and an inner region where the presence of the wall dominates and the velocity gradient is independent from the outer flow therefore presenting a self-similarity if correctly rescaled.

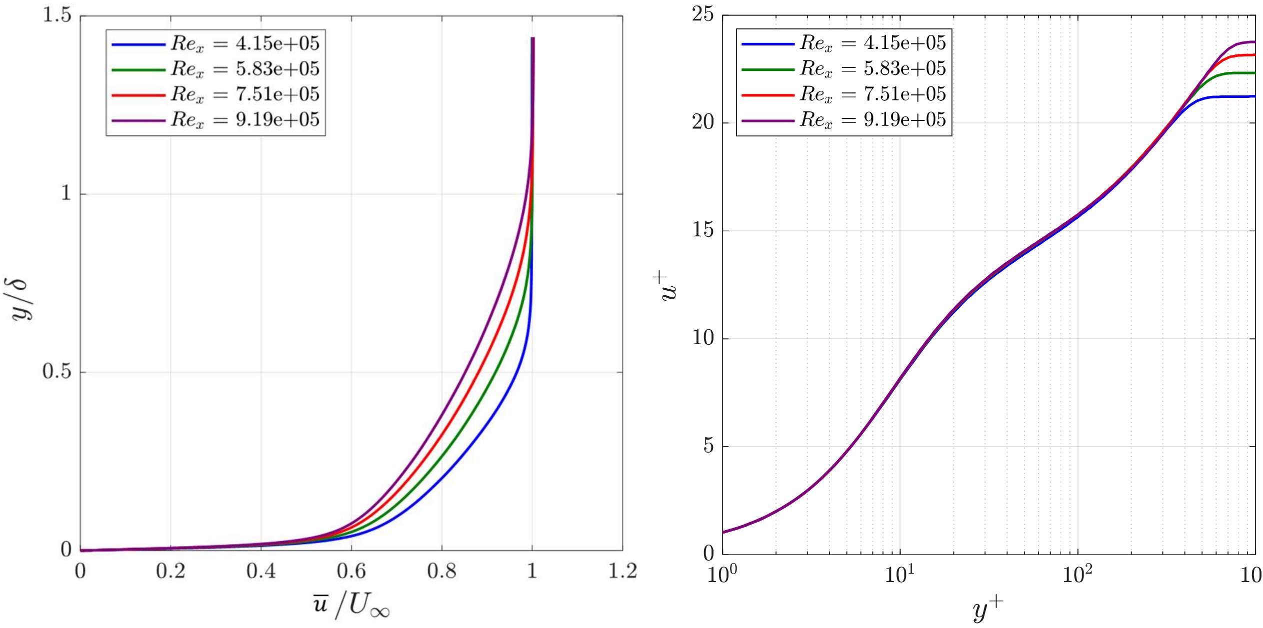

Figure 6 Mean streamwise velocity profile for fully developed TBL in ZPG conditions. Left: outer units. Right: inner units. Data from [12].

To better highlight said characteristic in the theory of wall bounded flows it is common to refer to so called wall units $y^+ = y/\delta_\nu$, $u^+ = \bar{u}/u_\tau$ which represent distance from the wall and streamwise velocity normalized with viscous scale.

When described by the non-dimensional wall units, the inner layer follows a universal law, known as the law of the wall:

$$u^+ = \overline{u}/u_\tau = f(y^+)$$

The outer layer, on the other hand, is described by using, a measure of the boundary layer's thickness, as the length scale and follows a wake function, which itself is dependent on the Reynolds number.

Focusing on the inner layer we can once again define three separate regions:

- Viscous Sublayer ($y^+ < 5$):
  - In this region situated very close to the wall the viscous forces dominate suppressing fluctuations and the flow can be considered laminar.
  - The mean velocity profile can be considered linear.
  $$u^+ = y^+$$
- Buffer Layer ($5 \le y^+ \le 30 \div 50$):
  - Above the viscous sublayer stands a transitional region where viscous and turbulent stresses are both significant.
  - This region shows a peak creation and dissipation in turbulent kinetic energy.
- Logarithmic Layer $30 \div 50 \le y^+ \overset{\sim}{<} 0.1\, \delta/\delta_\nu$:
  - The mean velocity profile is logarithmic:
  $$u^+ = \frac{1}{\kappa} ln(y^+) + B$$
  where $\kappa \approx 0.41, B \approx 5$ are respectively the Karman and Coles constant.

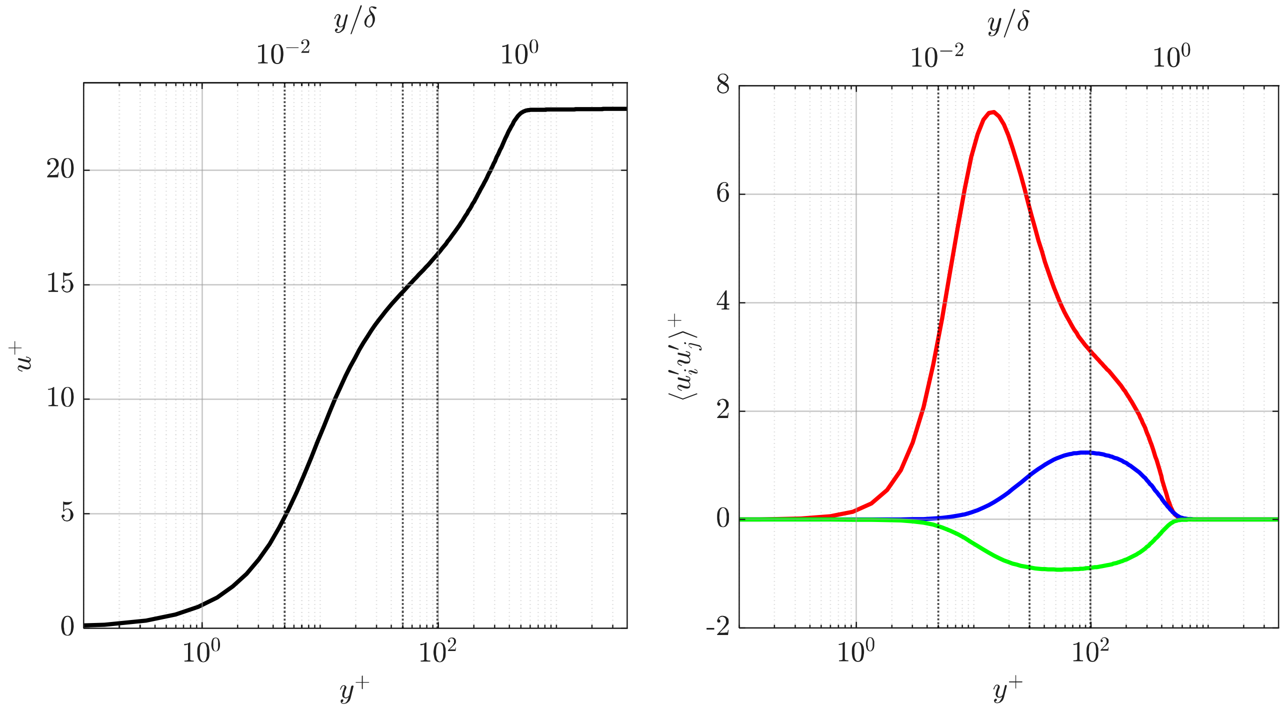

Figure 7 Left: Mean velocity profile in inner units. Dashed lines show the different regions previously described. Right: normalized Reynolds stresses distribution: $\langle u'u' \rangle^+$ (blue), $\langle u'v' \rangle^+$ (red), $\langle v'v' \rangle^+$ (green). *Data from [12].*

The self-similarity extends beyond the mean flow to the statistical fluctuations. In the inner layer, the Reynolds stress tensor components, when normalized by the friction velocity squared, collapse onto universal profiles.

For a fully developer TBL in ZPG, we can identify the following trends for the normalized stresses as a function of y^+:

- Streamwise Normal Stress ($\langle u'u' \rangle^+$):
  This component typically exhibits a distinct peak in the buffer layer ($y^+ \approx 15$) corresponding to the region of maximum turbulent kinetic energy production. It is associated with the violent "bursting" events of the near-wall cycle.
- Wall-normal and Spanwise Stresses ($\langle v'v' \rangle^+$):
  These components are smaller close to the wall but increase moving away from the viscous sublayer as the turbulence becomes more isotropic.
- Reynolds Shear Stress ($-\langle u'v' \rangle^+$):
  This term represents the vertical transport of streamwise momentum. It is negligible within the viscous sublayer but grows rapidly in the buffer layer, becoming the dominant stress term in the logarithmic region.

At wall fluctuations must be null and far from the wall tend to zero (or to the value characteristic of residual turbulence of the free flow)

2.2.2 Self-Sustaining Cycle

The complexity of a TBL is governed by a self-sustaining process known as Near-Wall Cycle in which two types of coherent structures, Low Speed Streaks (LSS) and Quasi Streamwise Vortices (QSVs), form between themselves a positive feedback loop.

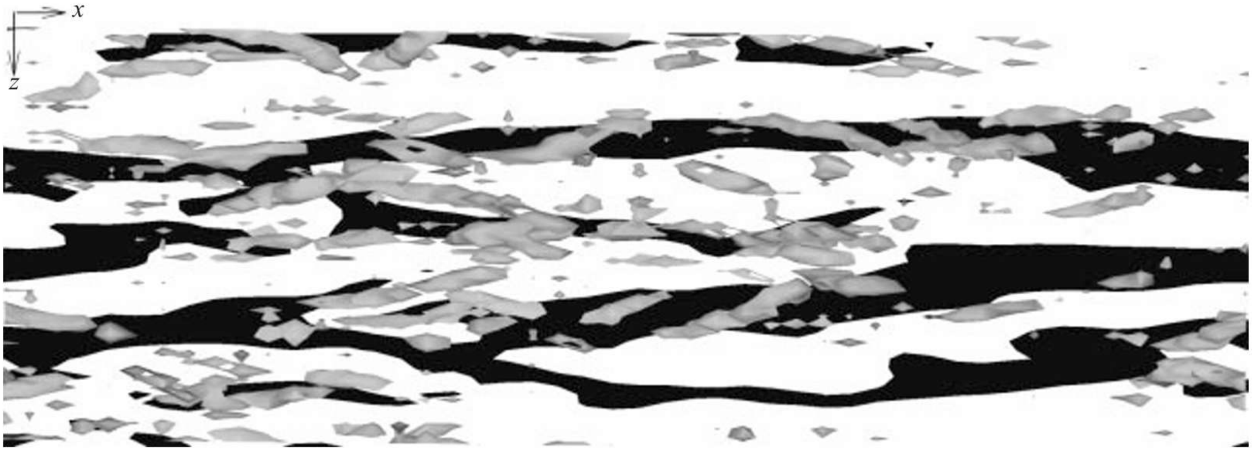

Figure 8 Top-down view of the near-wall region. Black, low-speed streaks; grey-shaded, streamwise vortices [13].

The streaks are elongated regions of uniform momentum that move downstream alternating in the spanwise direction a slower and faster speed than the mean flow. Quasi-Streamwise Vortices are structures of alternating vorticity oriented roughly in the streamwise direction, which reside in the buffer layer just above the streaks.

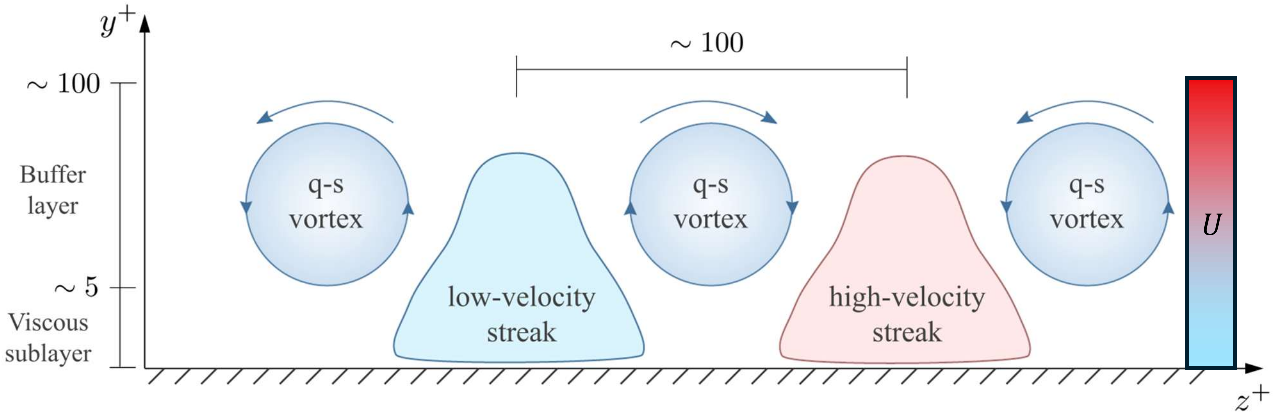

Figure 9 Schematics of the structures interacting in the near-wall cycle. Spanwise wall normal plane. Adapted from [14].

Due to their strong spatial coherence, the QSVs induce wall normal velocity to the streaks leading to ejections that lift low-momentum fluid away from the wall and sweeps of high-momentum fluid in the direction of the wall. As the streaks intensify, they become susceptible to instabilities leading to a breakdown that perturbs the local flow field, regenerating the quasi-streamwise vortices via non-linear interactions, thus closing the cycle [15].

While the Near wall cycle can persist with only streaks and QSVs, strong ejection events often bridge the gap to the logarithmic layer; when that happens a region of strong shear is detached from the wall and the resulting inflectional velocity profile becomes unstable to Kelvin-Helmholtz instability. The shear layer rolls up into a spanwise vortex 'head', connecting the QSVs ('legs') to form a Hairpin Vortex.

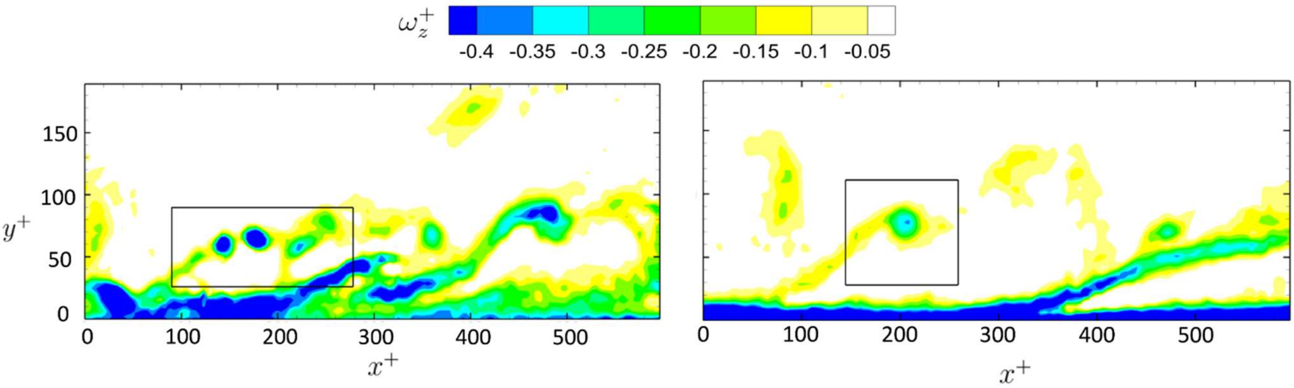

Figure 10 Identification of hairpin vortices; heads boxed, legs are following. Left: reference case. Right: flow control [6].

Hairpin vortices extend across a region of strong wall-normal shear, consequently, they undergo significant stretching and tilting, which leads to an intensification of the vorticity within their legs [17]. Through this mechanism, a primary hairpin can auto-generate new vortices upstream resulting in the generation of hairpin packets that are significant contributors to skin friction, as they facilitate large-scale momentum exchange across the boundary layer [17].

Since the NWC is the engine of turbulence production, the central hypothesis of drag reduction methods is that interrupting this cycle yields skin-friction savings.

CHAPTER III

Turbulent Drag Reduction

The current chapter serves as a review of the relevant concepts and literature on Turbulent Drag Reduction that are core to the understanding of the remainder of the thesis. After a brief introduction on the state of the art the focus is narrowed to spanwise wall forcing discussing the physical mechanism proposed in the literature, the actuation parameters and the effects on the mean velocity profile. Finally, the issue of spatial development across finite-length actuators is discussed identifying the current gap in the literature regarding a complete modelling of spatial development of the skin friction coefficient that this research aims to close.

3.1 State of the art

In the present work we define drag reduction as the change in friction drag obtained from an uncontrolled state:

$$\mathcal{R} = \frac{c_{f_0} - c_f}{c_{f_0}} \cdot 100$$

Effective drag-reduction strategies for Turbulent Boundary Layers target the high-momentum transport within the near-wall region. Control techniques that successfully dampen the Self-Sustaining Cycle described in previous the chapter result in reduced wall normal velocity fluctuations caused by ejections/sweeps. This reduction in turbulent mixing allows the mean velocity profile to sustain a smaller gradient at the wall which is synonymous with a reduction in the mean skin-friction drag.

Approaches to turbulent skin-friction drag reduction can be classified by the respective energy budget:

- Passive methods:
  This class of techniques alters the fundamental properties of the fluid or the fluid-surface interaction without the need of external energy.
  Canonical examples in the aerospace sector include: dimples [18], wavy walls [19] and riblets [20]. Among these, riblets, represent the state of the art in aviation, having reached a Technology Readiness Level of 9 in aeronautical applications, and providing a net drag reduction in the order of $\approx 10\%$ in laboratory conditions [8].

Figure 11 Passive surface modifications. Left: Riblets [21]. Right: superhydrophobic lotus leaf [22].

- Active methods:
  This class of techniques introduces external energy in the flow field, altering the flow characteristics by mechanical or electric-magnetic forcing. These methods can additionally be divided into:
  - Open loop:
    Where the forcing signal is predetermined and independent from the instantaneous flow field.
  - Closed loop:
    The forcing signal is defined in ‘real time’ depending on the flow field.

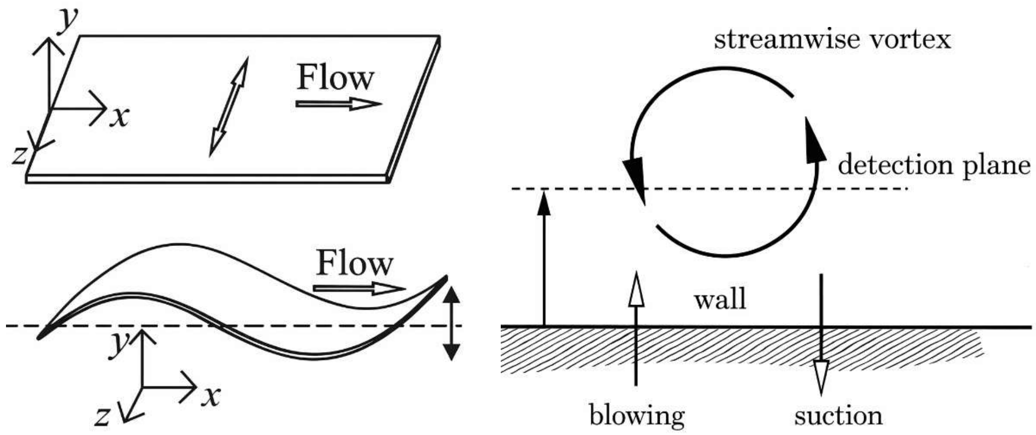

Figure 12 Schematics of active drag reduction methods. Left: wall oscillation and wall deformation (open loop)[16]. Right opposition flow control (closed loop); spanwise wall-normal plane [20].

While passive methods offer limited gains, achieving higher levels of drag reduction is possible with active control with measured drag reductions up to ~ 40% [6].

Here, the distinction between scientific success and industrial implementation becomes critical [23]. The practical implementation of such systems, especially in aviation, faces formidable engineering challenges due to the higher complexity, predisposition to mechanical failures above all, negative net energy efficiency. It is clear that for real world application in the aeronautical sector all active methods may eventually converge in a passive version of themselves.

3.2 Temporal spanwise wall forcing

By spanwise wall forcing we imply the imposition of a spanwise motion to the fluid occupying the near wall region. This can be achieved both through a purely temporal or purely spatial evolution or a combination of the two.

In this work the focus is solely on the most fundamental version of spanwise wall forcing, the imposition of a purely temporal sinusoidal oscillation of the wall in the spanwise direction. In this case the oscillation of the wall can be described as follows.

$$W_w(t) = W_m \cos\left(\frac{2\pi t}{T}\right)$$

Where W_m represents the maximum velocity and T the period of the oscillation.

This motion, coupled with the no slip condition, gives rise to a new shear layer called Stokes' layer that extends from the wall up to a certain height δ_z as a function of the actuation and flow parameters. The existence of this new shear layer and its interaction with the structures of the TBLs is considered the root cause of the modulation of drag incurred using this method.

Different explanations for such drag reduction exist in the literature; here we recall the idea of reduced spatial coherence. When the Stokes' layer is confined in the viscous sublayer or the lower region of the buffer layer, the spanwise velocity component imposed to the fluid leads to a decrease in the spatial coherence between the low speed streaks and the quasi streamwise vortices existing above them leading to fewer bursting events [8]. Additionally, this causes to a sudden shift between the legs, existing closer to the wall, and head, already detached, of the present hairpin vortices reducing their characteristic self-inducing behaviour [10].

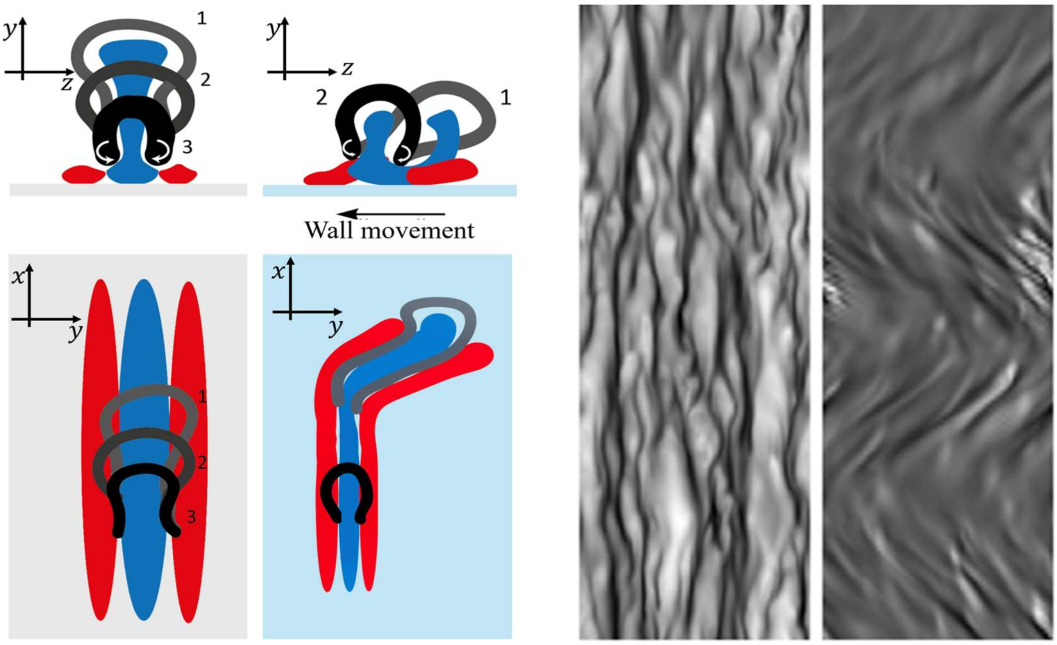

Figure 13 Left: proposed mechanism of reduced spatial coherence; adapted from [6]. Right: Instantaneous velocity fields in a plane parallel to the wall at $y^+ = 11$ *for the reference boundary layer and the oscillating case. The dark grey areas indicates low-speed regions and lighter shades indicate high-speed patches[24].*

3.2.1 Drag reduction and parametric space

Regardless of the physical mechanism, if the Stokes' layer extends past the buffer layer the imposition of this additional velocity component leads to an enhancement in the turbulence production.

It is clear that for all drag reduction purposes the Stokes' layer should not extend past the lower region of the buffer layer and therefore exist in a region where turbulence in non-significant. Starting from this assumption one can analytically infer the Stokes' layer thickness from the laminar flow solution considering the spanwise motion decoupled from the streamwise flow. Doing so it is shown a proportionality between the Stokes' layer penetration length and the period of oscillation $\delta_z \propto \sqrt{T}$

Once again, the relevant parameters to the case study are more commonly expressed in their non dimensional form, with a normalization in respect of the viscous units of the reference unactuated flow; more specifically, for an experimental campaign we define:

$$T_{osc}^{+} = \frac{T\, u_{\tau 0}^{2}}{\nu} \quad \cap \quad A_{osc}^{+} = \frac{A_{osc}}{\delta_{\nu}} \quad \Longrightarrow \quad W_{m}^{+} = \frac{\pi\, A_{osc}^{+}}{T_{osc}^{+}}$$

This description of wall forcing is used to accommodate the fact that in an experimental campaign the oscillation is often provided through a crank slider mechanism and, therefore, the parametric space available is limited by the frequency of oscillation $(1/T)$ provided by your source of power and the radius A_{osc} of the wheel used. In order to have an optimum penetration length of the Stokes' layer $\delta_z^+ = \delta_z/\delta_\nu \sim 6.5$, there exists an optimum range of T^+ which for a TBL has been found around $T^+ \in [60, 80]$; on the other hand there is a monotonic relation between oscillation velocity and drag reduction $\mathcal{R} \propto W_m^+$.

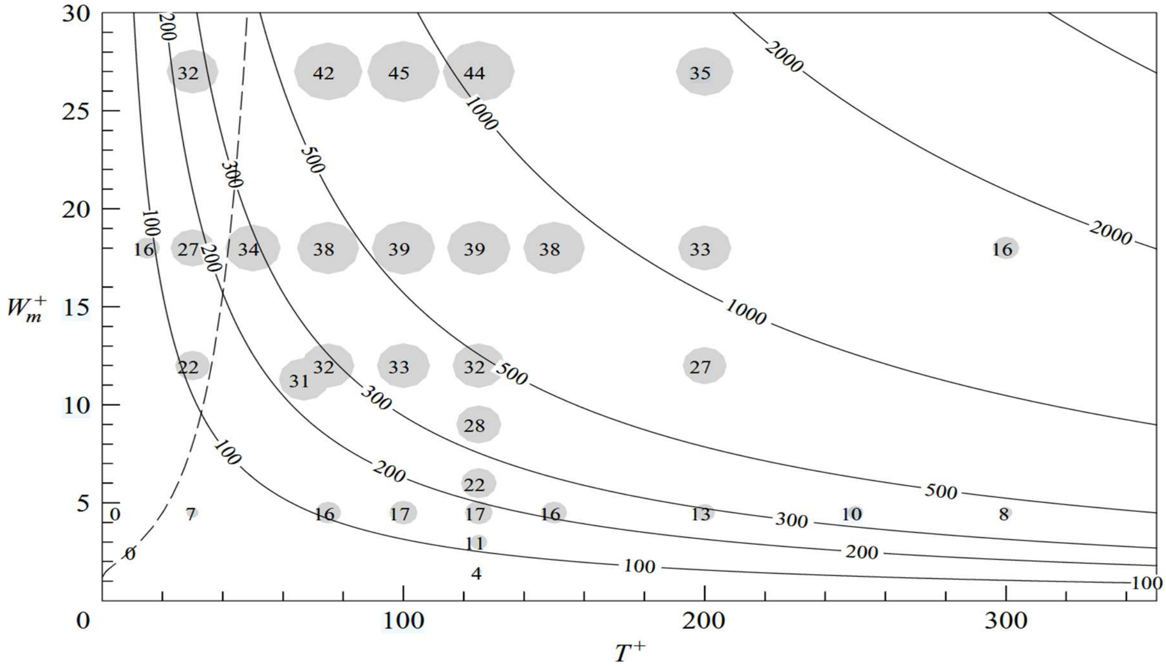

Figure 14 Quadrio's map. Drag reduction as a function of actuation parameters for channel flows (inner scaling) [25].

Considering this proportionality and the definition of W_m^+ the need for low free-stream velocity becomes evident. Since the friction velocity scales with the velocity of the free-stream, operating at lower Reynolds allows for higher drag reduction levels within the limitations of a given forcing system facilitating the experimental measurements.

3.2.2 Statistical description of Drag reduced Turbulent Boundary Layer

Flow control by spanwise wall forcing leads to significant changes on the functional form of the mean velocity profile of the TBL. As previously mentioned disrupting the near wall cycle allows for a sustained lower mean velocity in the near wall region leading to a viscous sublayer of increased physical size.

As described by Skote [26], when the mean velocity profile is scaled with the actual friction velocity and viscous length scale, the linear region is unchanged while the logarithmic layer is affected by a change in intercept and slope. More specifically the intercept shift follows a linear relation with the DR while Von Karman's constant is proportional to the ratio of actual friction velocity and the one of the reference case therefore being reduced for higher Drag Reduction levels.

$$k_r = k_0 \cdot r$$

$$B_r = B_0 + k_D \cdot DR$$

With $r = u_\tau / u_{\tau,0}$ and k_D found to be constant ≈ 9.

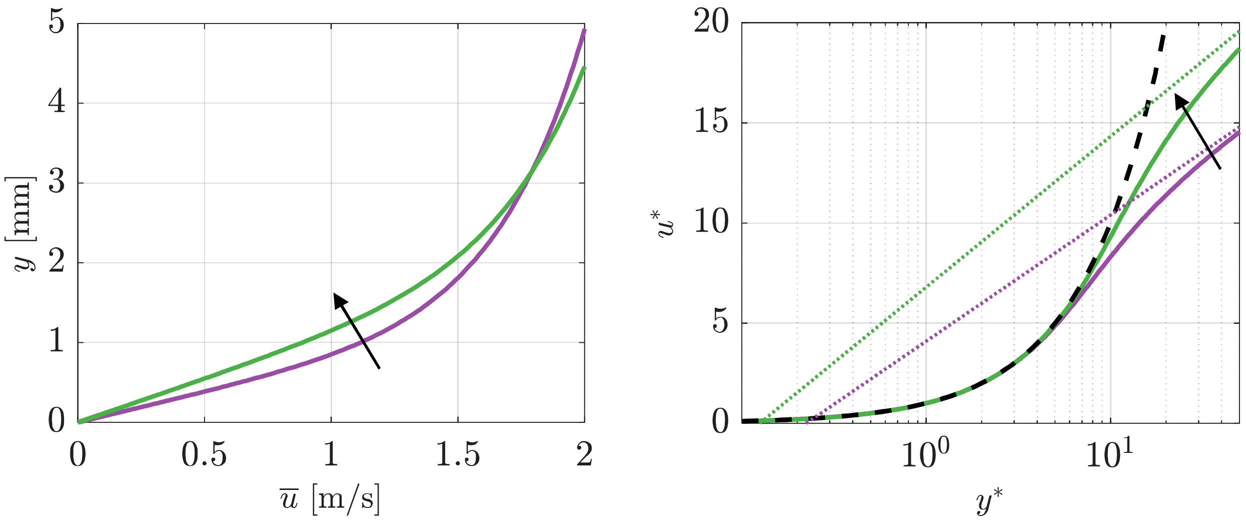

Figure 15 Mean streamwise velocity profile for the refence (purple) and controlled (green) case. Left: physical units. Right: inner units highlighting common linear region (black) and difference in logarithmic law. Reconstructed from Skote equations and Spalding low for the inner layer.

3.2.3 Finite actuator effects

Unlike in DNS simulations, where streamwise-homogeneous flow fully adapted to the drag reduced state are often studied, a boundary layer developing over a finite length actuator is dominated by spatial transients:

- Adaptation Transient:
  This is the region where the flow adapts to the forcing motion and the drag reduction rises from zero to its maximum level. There is a strong consensus that the initial response is relatively rapid with multiple studies showing that $\sim 75\%$ of the total friction change occurs within the first boundary layer thickness while the full, maximum drag reduction is typically achieved within 3 to 5 boundary layer thicknesses [27].

- Recovery transient:
  The relaxation of the TBL downstream the actuated section is generally reported to be an even faster process. Numerical and experimental studies show the drag reduction effect being reduced by 80% after just one boundary layer thickness and disappearing entirely by 2δ [27].
  Additionally, some studies report a slight "drag overshoot" where the local skin friction exceeds baseline value after the recovery [26]. This is at least partially explained by the different boundary layer thicknesses between the controlled and reference cases at the same streamwise position.

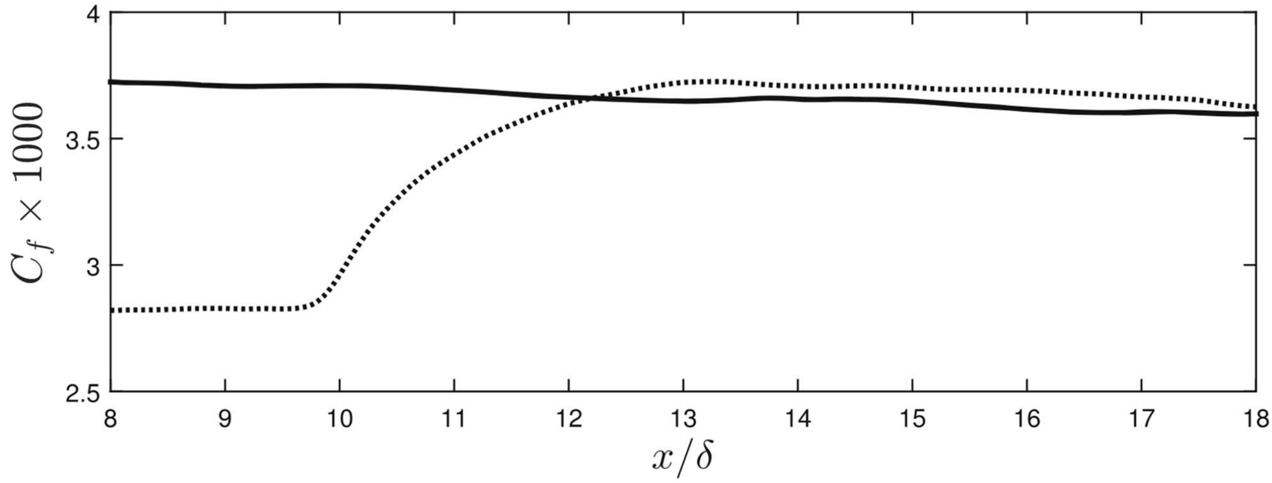

Figure 16 DNS data for skin friction coefficient recovery transient [26].

Previous studies have identified a characteristic shape of the drag-reduction curve $\mathcal{R}(x)$ typically following an exponential evolution towards a new regime after the onset and offset of wall forcing [27].

This behaviour has been modelled for the first transient through a simple single exponential law inspired by linear systems theory [28]. In such model the skin friction response is treated as a first-order system reacting to a step-like forcing allowing for the definition of a spatial length scale ξ that governs the evolution of $\mathcal{R}(x)$ from its unperturbed to its asymptotic value. This spatial length scale is defined as the distance after which the change in C_f has reached $1/e$ of its maximum value.

Following this line of thought, the present work extends the conceptual framework by adapting said response model for the second transient, aiming to capture the full streamwise evolution of the friction coefficient and giving insight on both the adaptation length and spatial memory of the system. Considering the reference coordinate system to start at the Leading Edge of the oscillating plate and L to represent its length, the complete model can be described as follows:

$$\begin{cases} C_f(x) = {C_f}_0^{up} - \left({C_f}_0^{up} - C_{f_c}\right)\left(1 - \exp(-x/\xi^{up})\right) \\ C_f(x) = C_{f_0}^{down} - \left(C_{f_0}^{down} - C_{f_c}\right)\exp\left(-(x - L/\xi^{down})\right) \end{cases} \qquad \xi = x \;\; t.c. \quad \Delta C_f(x) = \Delta C_f^{tot}/exp$$

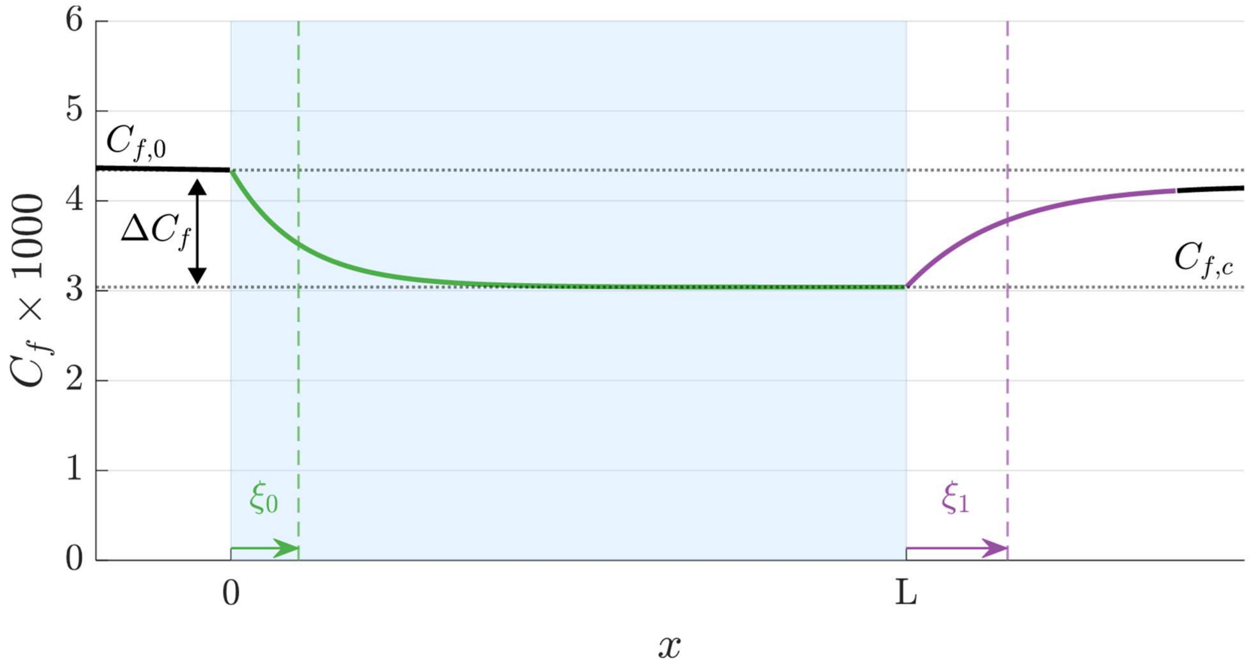

Figure 17 Proposed modelling for the spatial transients. Skin friction coefficient across oscillating plate.

This extended formulation provides a complete foundation for evaluating the spatial response and memory of the drag reduction effect and motivates the methodology presented in the following sections.

3.2.4 Research questions: Turbulent Drag Reduction

While a significant portion of the present thesis is dedicated to the analysis and development of novel modelling techniques needed to overcome experimental limitations of near wall velocimetry, the ultimate objective of the thesis is to leverage said developments on the metrology side to investigate fundamental questions on the physics of skin friction reduction through spanwise wall forcing.

More specifically the present work focuses on the spatial response of the TBL to the flow control techniques and aims to answer the following research questions:

1. Modelling of the spatial response:
   Can the streamwise evolution of the skin friction coefficient be accurately described by a simple single exponential function? Making use of the high streamwise resolution this thesis investigate whether the recovery transient present the same exponential form proposed by recent publications for the adaptation transient [28].

2. Quantification of the spatial memory of the flow:
   What is the characteristic length scale of the recovery transient downstream the actuated region? By fitting the proposed model to the experimental data a characteristic length scale is easily defined. Understanding the spatial persistence of the drag reduction effects is crucial for the development of future passive drag reduction techniques.

CHAPTER IV

Particle Image Velocimetry

Particle Image Velocimetry has been the measurement technique of choice used for this research. The following chapter provides a comparative assessment of the different experimental techniques available for wall-shear stress measurements justifying this choice. The fundamental principles of PIV are then detailed in order to allow for a better understanding of the measurement technique in and of itself as well as challenges posed by the analysis of wall-bounded flows with PIV.

4.1 Wall shear stress measurement techniques

Experimental techniques for skin friction evaluation are categorized into direct methods, which measure the shear force mechanically, and indirect methods, which infer shear stress at wall via pressure gradients, heat transfer analogies, optical techniques or velocity diagnostics. The specific experimental constraints of this study though preclude the majority of these standard techniques.

Technique	Vibration Sensitivity	Spatial Resolution (x)	Repositioning Flexibility	Spatial coverage
Floating Element	Critical	Very Low	Very Low	High
Oil-Film Interferometry	Critical	High	Low	Very Low
Hot-Film Anemometry	Medium	High	Very Low	Medium
Hot wire	Medium	Very High	High	Very Low
PIV	Low	Very High	High	High

Table 1 Skin friction measurement techniques compatibility with experimental constraints

First of all, the active mechanical forcing introduces significant vibration and inertial loads, rendering unfeasible the use of techniques relying on physical sensors directly in contact with the oscillating plate.

Secondly, the investigation focuses on the spatial development of the TBL, consequently, global integral measures cannot be used; it is important to have a technique with high spatial resolution. Velocity based diagnostics is therefore deemed as the most appropriate approach; these techniques evaluate the skin friction coefficient by relating the measured streamwise velocity profile to the wall shear stress.

Lastly, we also have to consider that the domain of interest for this study poses a significant challenge in and of itself; considering the interest in a portion of $\sim 1m$ the measurement technique of choice should allow for ease of repositioning.

Considering the experimental constraints previously described, Particle Image Velocimetry has been selected as the measurement technique of choice. Still, measuring the spatial evolution of skin friction from PIV measurements is not an easy task and required the use of novel approaches that would suit the specific needs.

4.2 Particle Image Velocimetry

Particle Image Velocimetry or PIV is a broad term used to define a family of non-intrusive techniques that allow for the investigation of a ‘global’ instantaneous flow field. The working principle is to capture the position of ensembles of tracing particles at different instants and, assuming negligible particle acceleration during the time separation, to infer their instantaneous speed by statistical analysis.

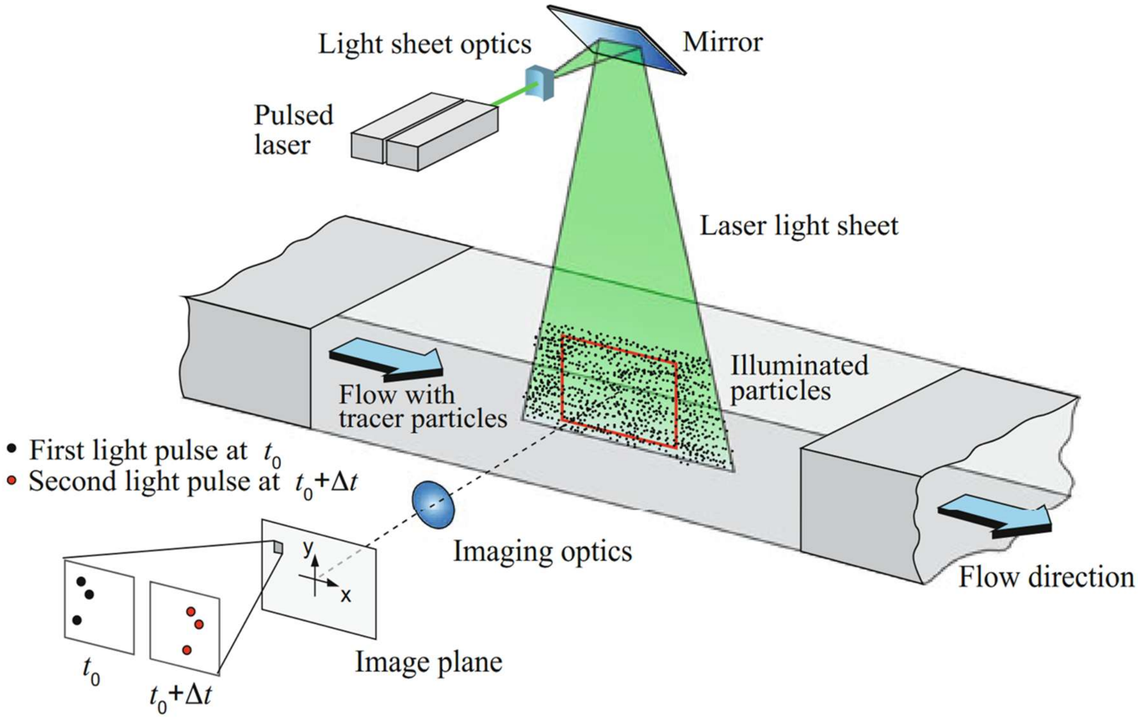

Figure 18 Typical planar PIV set-up [29].

Depending on the type of experiment being carried out double exposure PIV can be divided in different techniques; more specifically one can define different types of PIV base on the target domain and velocity components to analyse as well as the time resolution.

As for the target domain/velocity components we can define:

- Planar PIV ($2D-2C$):
  This is the standard configuration. It measures two velocity components (2C) within a single 2D plane. It requires one camera, typically mounted normal to the laser sheet.

- Stereo PIV ($2D-3C$):
  This technique measures all three velocity components (3C) within a single 2D plane. It requires two cameras viewing the plane from different, calibrated angles (using the Scheimpflug principle) to reconstruct the out-of-plane component.

- Tomo PIV ($3D-3C$):
  This measures all three velocity components (3C) within a 3D volume. It requires three or more cameras to reconstruct the 3D particle distribution, representing a significant increase in experimental and computational complexity.

As for the time resolution one can divide PIV techniques in:

- Low speed (non-time resolved):
  Acquires image pairs at a low repetition rate (i.e., $1 \div 15\ Hz$). The time between pairs is long, meaning each velocity field is statistically independent.
- High speed (time resolved):
  If the acquisition frequency is higher than a certain value defined as function of the characteristic timescale of the events of interest it allows for the investigation of the temporal evolution.

In order to retrieve information regarding the spatial evolution of the time averaged skin friction it is sufficient to target the wall normal streamwise plane; additionally in this investigation we are not interested in a temporal evolution but only on the spatial evolution of the flow. For these reasons, non-time resolved planar PIV has been performed with some caveats in order to account for the forcing technique when setting the acquisition parameters.

4.2.1 Seeding, illumination light delivery and sensors

Tracers must present the correct dimensions and density to be able to follow the fluid and all the structure of interest inside the flow field.

On the temporal side this concept can be exemplified by a study of the Stokes number of a given system tracer-fluid which can be defined as the relaxation time of the tracers (τ_p) on the characteristic timescale on interest of the flow (τ_0).

Considering a simplified model of a solid spherical particle of diameter d_p and density ρ_p immersed in a fluid flow with a timescale τ_0 and viscosity μ_0 we can redefine the Stokes number as follows [19]:

$$St = \frac{\tau_p}{\tau_0} = \frac{d_p^2}{18}\frac{\rho_p}{\mu_0}$$

If the Stokes number is small $(St \ll 1)$ we can consider the tracer as a passive scalar (from a purely dynamics standpoint). On the other hand, if the Stokes grows $(St \sim 1)$ the inertia of the tracer makes it so it’s the velocity is correlated to the fluid but ignores the smallest fluctuations. The opposite case $(St \gg 1)$ can be described as the projectile motion.

As previously mentioned a light source is needed to illuminate the tracing particles; despite the recent interest in LED [30] and continuous laser, dual cavity pulsed lasers still represent the state of the art for PIV in wall bounded gaseous flows.

Lasers are widely used in PIV, due to their ability to emit monochromatic infrared light with high energy density, which can easily be bundled into thin, light sheets/volumes allowing to record the tracer particles without chromatic aberrations. For a $2D - 2C$ PIV setup the light beam coming from the laser has to be shaped into thin light sheets with a thickness of $\sim 1\ mm$.

Many are the sensor available today for Digital Image Recording, but for PIV applications the most common are Charge Coupled Devices (CCD), and Complementary Metal-Oxide Semiconductor (CMOS) devices; these sensors convert the light into electric charge, which is further converted into voltage and the stored digital signal. Historically the CCD has found the most widespread use, however in recent years CMOS sensors have rapidly improved in regards of technical parameters such as Signal to Noise Ratio (SNR) and resolution, as well as costs and robustness.

4.1.2 Camera optics and time resolution

Independently from the type of sensor used during the recording particle image is projected to a certain position in the sensor; the mapping from the physical Field of View (FOV) to the sensor is defined by the magnification (M) of the set-up.

$$\begin{pmatrix} X \\ Y \end{pmatrix} = M \begin{pmatrix} x \\ y \end{pmatrix}$$

The magnification factor can be defined as the distance between sensor and lens plane (z_0) over the distance between object and lens plane(Z_0) or the sensor size over the FOV; the higher the magnification the more zoomed in the image will be.

$$M = \frac{z_0}{Z_0} = \frac{pixel\ pitch \cdot n\ pixel}{FOV}$$

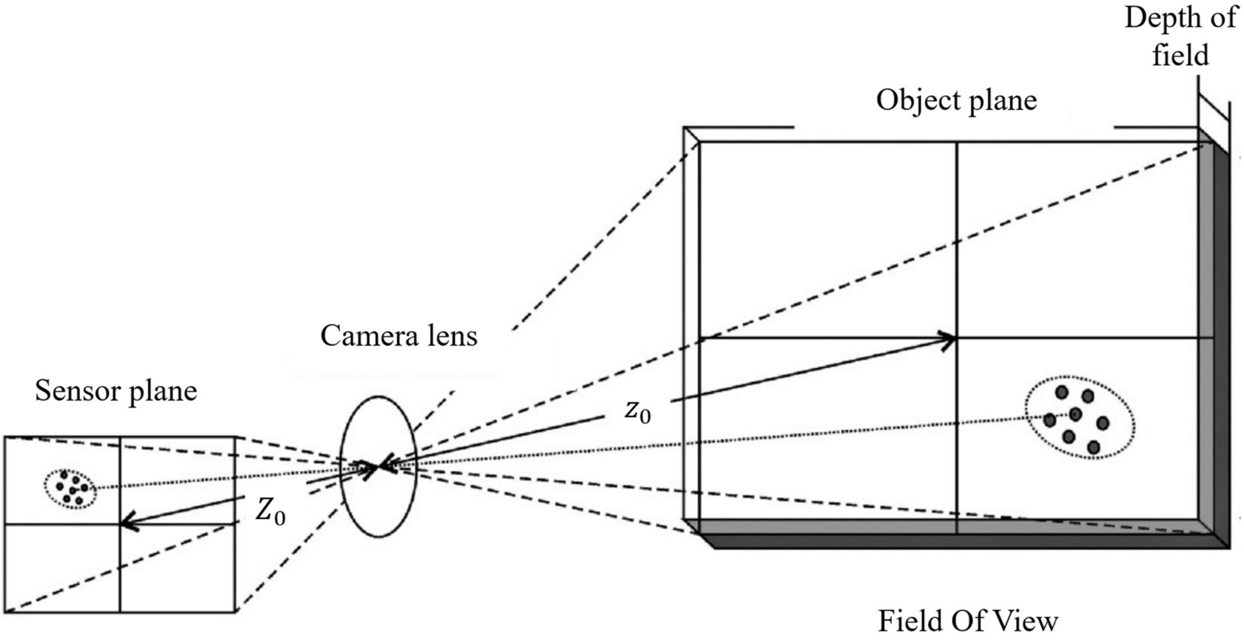

Figure 19 Schematics of image projection, adapted from [31].

Other essential parameters to describe the optic lenses are:

- Depth Of Field (δ_z):
  - This is the depth around the target plane that appears acceptably sharp or in focus.
  - For 2D-2C PIV it has to be greater than the laser thickness to ensure all illuminated tracers are in focus and can be estimated as:

$$\delta_z = 4.88\, \lambda f_\#^2 \left(\frac{M+1}{M}\right)^2$$

- F-stop $(f_\#)$:
  - This is the ratio of the focal length (f) and aperture diameter (d) of the camera.

$$f_\# = f/d$$

  - It regulates the Depth Of Field $(\propto f_\#^2)$, brightness $(\propto f_\#^{-2})$, and resolution of the system$(\propto f_\#^{-1})$.

Other significant parameters in PIV are related to timing of illumination and image acquisition; more specifically we can define:

- Pulse separation (Δt):
    - This is the temporal separation within the couples of snapshots.
    - It is directly related to the movement of the tracers: increasing the pulse separation increases the SNR but also increases the risk of loss of information due to out of plane motion and weakens the assumption of linear motion.

- Acquisition frequency $\left(f_{acq}\right)$:
    - This parameter represents the time separation between different couple of snapshots.
    - It is crucial for time resolved PIV as well as to guarantee decorrelation of the acquisition for non-time resolved case studies.

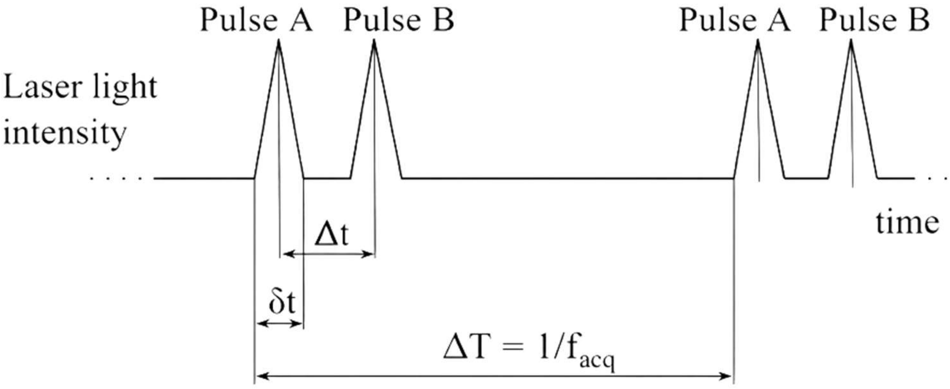

Figure 20 Visual representations of PIV acquisition parameter [10].

4.1.3 Working principles

Once the image acquisition is complete, the PIV algorithm reconstructs the instantaneous velocity field by statistically analysing pairs of consecutive snapshots (A, B) of intensity I, I'. The process begins by discretizing the FOV into a structured grid (m, n) defined by the user. This process divides the image into small sub-regions known as Interrogation Windows (IW), each isolating a local ensemble of seeding particles.

In its fundamental implementation, the algorithm compares the particle pattern's position (i, j) within of each IWs of the first snapshot to the corresponding in the second snapshot. This comparison is performed via normalized spatial cross-correlation, which statistically determines displacement (ξ, η) as the 'best match' for the particle pattern's new location.

$$c(m,n) = \frac{\sum_{i,j \in IW} \left[I_A(i,j) - \bar{I}_A \right] \cdot \left[I_B(i+\xi, j+\eta) - \bar{I}_B \right]}{\sigma_{I_A} \sigma_{I_B}}$$

By identifying the displacement corresponding to the maximum cross correlation coefficient, the average shift of the particles within the window is quantified; since the temporal separation is fixed, the velocity in the image plane is easily derived. Finally, the optical magnification factor is applied to convert these pixel-based measurements into the physical flow velocity vector.

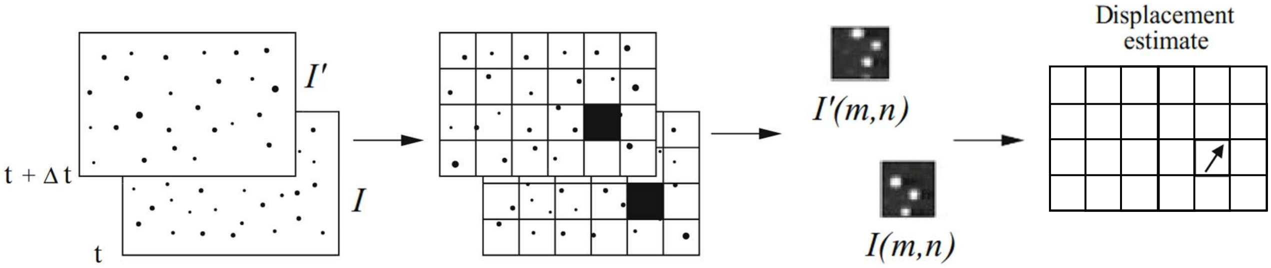

Figure 21 Visual representation of cross correlation algorithm. Adapted from [18].

While this brief overview explains the basics of the mathematical modelling of PIV, modern implementations employ iterative Window Deformation and Sub-pixel Interpolation to resolve displacements with accuracies below 0.1 pixels, accommodating the strong shear and rotational gradients present in wall turbulence; for more information regarding PIV and its implementations refer to [29].

4.1.4 Challenges in Wall bounded flows

Using PIV for wall bounded flows presents some significant challenges in the acquisition of accurate data in the near wall region.

Due to the intrinsic nature of cross correlation, the velocity measured for each IW is determined as the spatial average of the particles present in said IW; being this a linear operator the measurement will be exact only if the velocity profile within the IW is linear and the distribution of particles homogenous. Close to the wall the mean velocity profile presents maximum curvature leading to a systematic bias error that can be described as a smoothing effect. Additionally, for vectors closer to the wall than half of the wall normal IW size (h), part of the interrogation window extends across the wall therefore including region where the velocity profile measured has no real meaning for the fluid itself causing a significant bias error which, depending on the presence or absence of reflections can either be positive or negative.

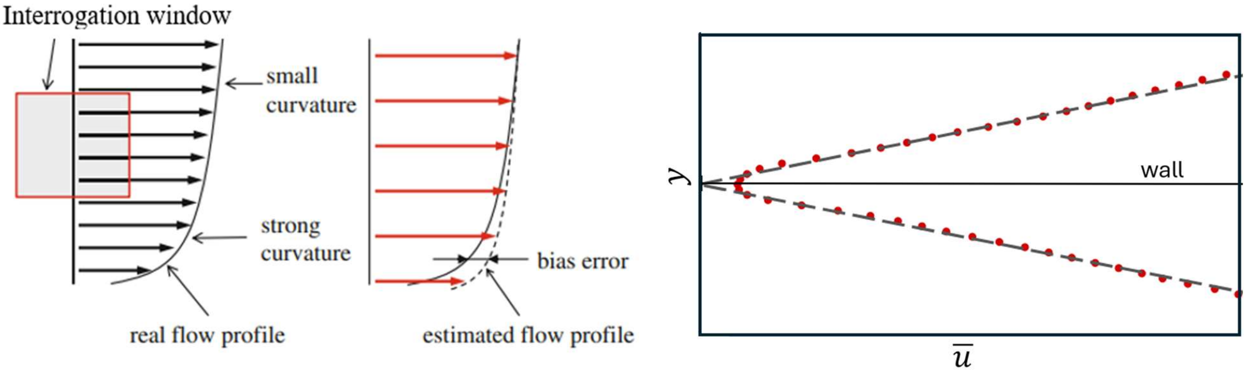

Figure 21. Left: spatial filtering effect of cross correlation [32]. Right: bias error in the near wall region; adapted from [33].

Finally, close to the wall, many different phenomena combine to create a significant noise floor reducing the SNR. More specifically, the presence of laser flare, and reflections if present, saturate the images in the near wall region rendering tracers identification more complex. Additionally, close to the wall, the fluid flows at a significantly lower mean velocity leading to a reduced particle displacement and increasing the sensitivity to random errors. Finally the tracers themselves are not dispersed in an homogeneous manner close to the wall. All the aforementioned reasons combined explain the reasoning behind the exclusion of velocity vectors at $y^+ < \max(2,\ 0.5 \cdot h/\delta_v)$.

4.1.5 Wall detection

In order to articulate on the velocity field resulting from PIV, in the context of wall bounded flows, it is important to precisely evaluate the wall coordinates as it serves as the ideal reference point. In most PIV experiments the wall position can be inferred from Mirror Image Symmetry methods [33]. The tracing particles and their reflections on the wall surface can be considered symmetrical in respect to the wall; therefore, the wall position coincides with the axis of symmetry between the real flow field and the reflected one.

However, as detailed in the previous section laser flare and surface reflections are the significant sources of error close to the wall; to mitigate these effects and achieve an acceptable SNR for velocity cross-correlation, it is standard practice to accurately align the laser as tangent to the wall and treat the wall surface with opaque, light-absorbing finishes (e.g., matte black coatings) [29]. While the suppression of reflections improves the measurement quality, it effectively eliminates the reflections needed for the Mirror Image Symmetry methods rendering wall identification non trivial.

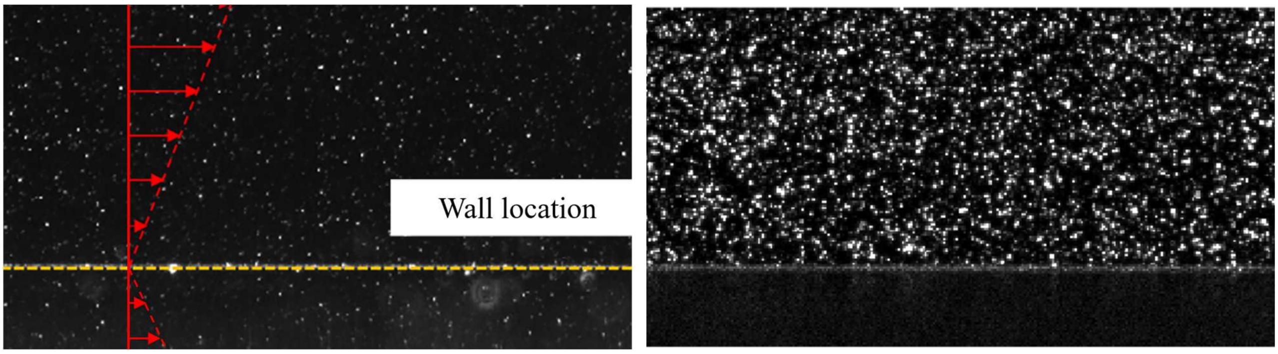

Figure 22 Left: Mirror Image Symmetry[33]. Right: absence of reflections.

4.3 Research questions: Wall-shear stress evaluation

The limitations discussed in this chapter pose significant challenges to the accurate estimation of the wall shear stress. In order to close the research gap highlighted in section 3.2.4 overcoming this hurdles is crucial; to do so a large part of the present work focuses on a novel metrology approach.

For said part of the thesis the main research questions tackled are the following:

1. Wall shear stress evaluation from PIV data:
   Is it possible to accurately recover wall-shear stress from velocity measurements in absence of reliable data close to the wall and minimal modelling efforts? Standard methods rely on high wall normal spatial resolution or a high degree of modelling on the functional form of the TBL; in this thesis a novel near-wall modelling approach first proposed for non-canonical flows [34], is analysed.

2. Accuracy and robustness to random error and wall position uncertainty:
   How does the proposed method perform when dealing with inherent measurement noise and bias error of PIV? As delineated in this chapter PIV data is subject to significant random and bias error in the near-wall region; this research aims to quantify the sensitivity of the proposed model to these error sources compared to traditional techniques.

3. Wall detection from flow field:
   Is it possible to precisely infer wall position solely from the mean velocity profile? Identifying the exact wall location is an important step of any PIV experiment; usually this is achieved by using external information or the presence of tracers reflections but what can be done in their absence?

CHAPTER V

Skin friction diagnostics

This chapter describes the data analysis techniques most commonly used to evaluate wall-shear stress from PIV data. Due to the low Reynolds number and non-equilibrium flow the discussion focuses on a local gradient based approach. Different models are introduced and critiqued, starting from a simple finite difference, to the commonly used linear fit; finally, a novel non-linear modelling approach based on the Arctangent function is proposed. This formulation aims to extend the fitting domain well beyond the viscous sublayer allowing for a more flexible use and higher robustness against the experimental constraints described in previous sections.

5.1 State of the art

Velocity based diagnostic techniques can be divided into two categories:

- Profile fitting methods:
  Methods such as the Clauser Plot and Composite Profile [35], rely on ‘a priori’ knowledge of the whole mean velocity profile of a canonical TBL and use this knowledge to fit parametric description of said profile to experimental data inferring the boundary layer characteristics.
  They represent the standard benchmark for precise experimental measurements and characterization of canonical ZPG TBL.
- Near Wall methods:
  These methods determine the skin friction locally by directly resolving the velocity gradient within the viscous or buffer layer, independent of outer layer assumptions. While physically sound and requiring minimal modelling efforts, this group of methods is more sparsely used due to the inherent high spatial resolution required for robust measurements.

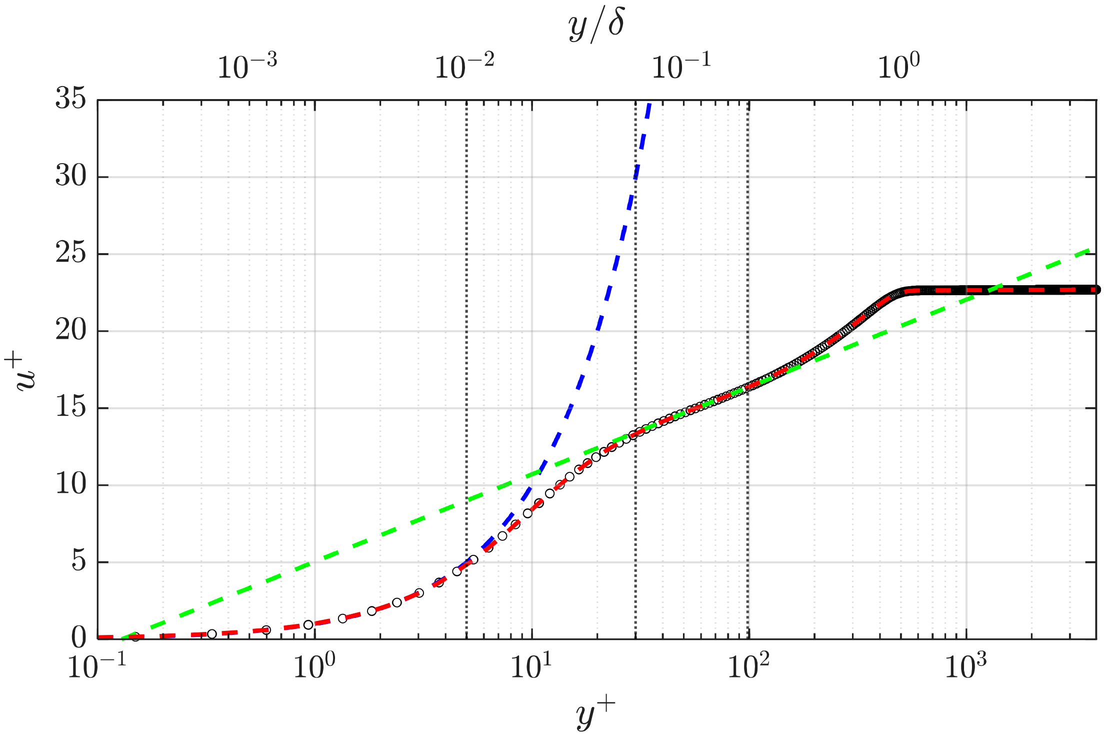

Figure 23 Mean velocity profile of a fully developed TBL (black dots) in inner units with superimposed different profile fitting and near wall models. Linear fit (dashed blue); Clauser fit (dashed green); Composite fit (dashed red). Data from [12].

The former family of methods, while robust for most canonical TBL, is ill-suited for the present study due to several reasons. Firstly, the low freestream velocity needed to obtain optimal forcing parameters for DR limits to low Reynolds numbers causing the extension of the logarithmic layer, if present at all, to be very limited. Secondly, as described in section 3.2.2, the imposition of spanwise wall forcing causes the constants defining the logarithmic region (k, B) to change as function of the drag reduction.

This study adopts the near wall local approach. As previously mentioned the working principle is to allow for an accurate reconstruction of the mean velocity profile at wall and infer the skin friction coefficient as follows:

$$C_f = \frac{\tau_w}{\frac{1}{2}\rho U_\infty^2} = 2\frac{\nu}{U_\infty^2}\frac{\partial \overline{u}}{\partial y}\bigg|_w$$

Considering the interest on the velocity gradient at wall and the shortcomings of PIV detailed in the previous chapter it is clear that, while conceptually straightforward, this approach presents its own set of problems. In the following section we discuss commonly used approaches and a novel approach developed to tackle said limitations [34].

5.2 Near wall velocity diagnostics

In a perfect world, once reconstructed the mean velocity profile, the gradient at wall could be directly inferred via first order finite difference for any two vectors residing within the viscous sublayer. However, it is clear that such approach would prove to be an ill conditioned problem with the spatial derivative acting as a high pass filter amplifying measurement error in the particle detection as spatial separation is reduced.

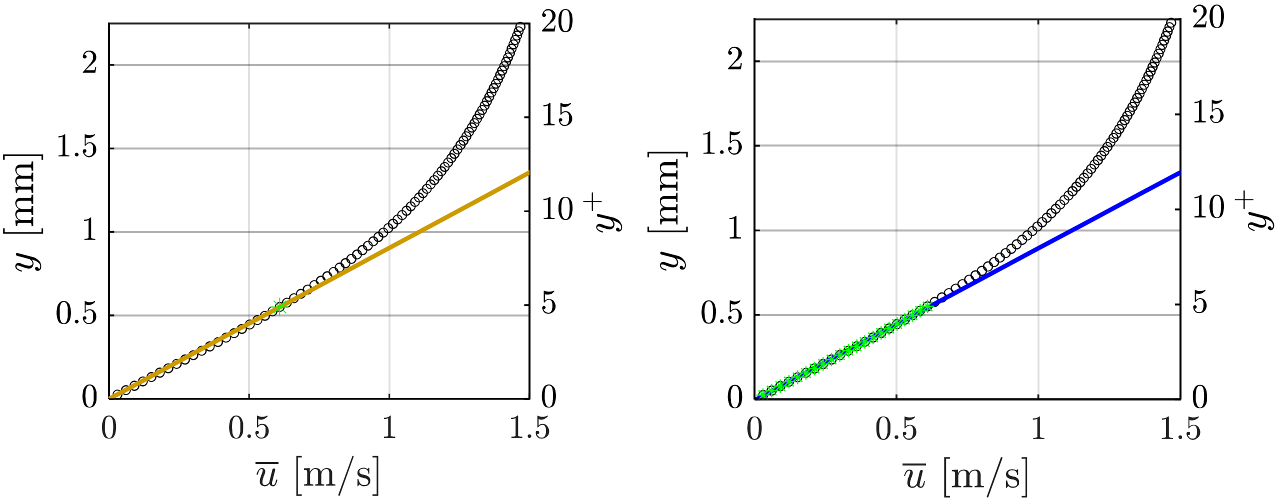

Figure 24 Visual representation of Finite differences (yellow) and Linear fitting(blues) on DNS data.

In order to improve the robustness of the two points interpolation to random noise, the standard approach is to use a linear regression over an increased number of measurement points within the viscous sublayer. The idea is that by increasing the number of independent measurements [1] used the effect of the random measurement errors is reduced. When paired to high resolution PIV or PTV capable of fully resolving this region this approach represents the benchmark for near wall local skin friction evaluation. Still, due to the finite size of the viscous sublayer, the number of measurement points available is often limited leading to a lower increase in robustness than expected.

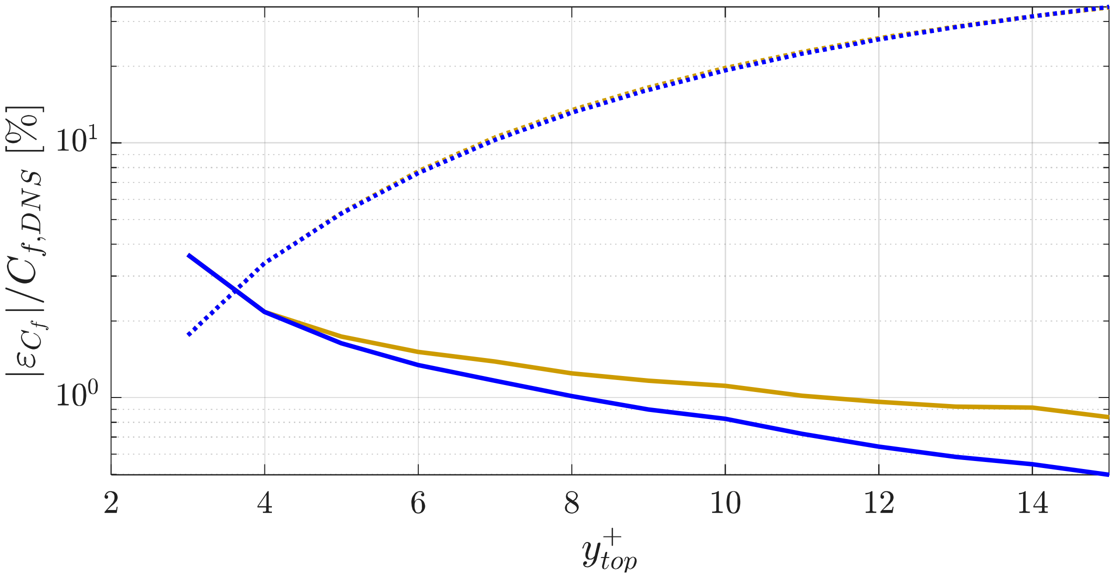

Figure 25 Relative error magnitude percentage for Finite differences (yellow) and Linear fit (blue) on DNS data with superimposed gaussian noise. Dashed lines (--): bias/truncation. Continuous line (-); random error.

---

[1] In PIV the wording 'independent measurements' has to be considered keeping in mind the concept of window overlap.

In order to increase the number of measurement points available it is necessary to make use of model capable of extending outside the viscous sublayer. To do so, non-linear fitting making use of higher-order polynomial models have historically been considered. These models are able to appreciate the non-linearity of the mean velocity profile therefore significantly reducing truncation errors and extending the kernel of points available for the fitting procedure. At the same time, simply increasing the polynomial order would increase the Degree Of Freedom of the fit leading to significant stability penalties and possibly overfitting problems. Additionally, any polynomial fit fails to capture the physical asymptotic behaviours of the TBL therefore reducing robustness when using points where this behaviour becomes appreciable.

In order to address both the need for an increased fitting kernel of points and robustness an Arctangent fitting model is proposed.

$$\overline{u}(y) = \mathrm{atan}(y)$$

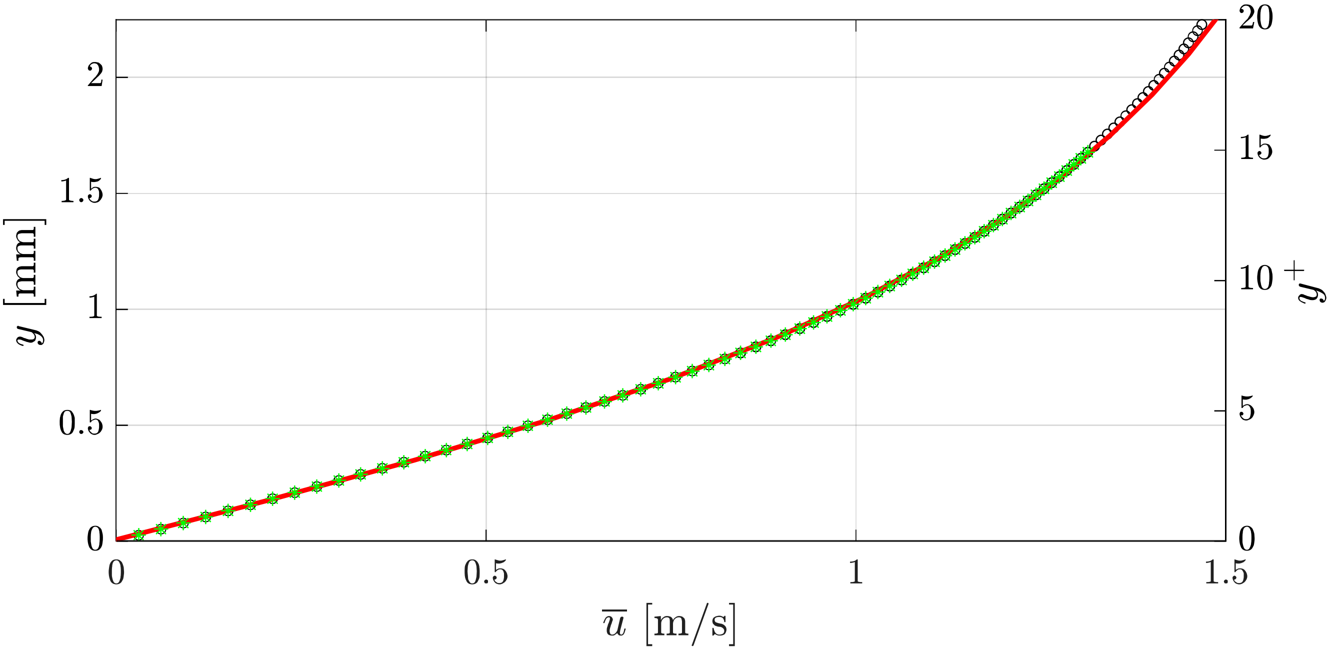

Figure 26 Visual representation of non-linear fitting with Arctangent model (red).

5.2.1 Arctangent fit

Although this non-linear fit lacks a direct physical derivation, it captures some of the key characteristics of the TBL mean velocity profile allowing for the use of points outside the linear region with a slower loss of accuracy thereby increasing the robustness of the fit.

The arctangent function has been originally proposed in the literature thanks to its consistency with some of the TBL's main features [34]:

- Vanishing at wall:
  The function vanishes at wall allowing to recover the no slip condition.
  $$\lim_{y \to 0} u(y) = 0$$
- Linearity at the Wall:
  The curvature of the function is null at wall recovering the linear behaviour of the mean velocity profile within the viscous sublayer.
  $$\left.\frac{\partial^2 \overline{u}}{\partial y^2}\right|_{y=0} = 0$$
- Monotonicity and Curvature**:**
  The function is monotonically increasing with respect of the wall normal coordinate.
  $$\frac{\partial \overline{u}}{\partial y} = \frac{1}{1+y^2} \geq 0 \quad \forall y \in [0, \infty]$$
- Asymptotic behaviour:
  The function exhibits an asymptotic behaviour mimicking the vanishing gradient of the mean velocity profile away from the wall.
  $$\lim_{y \to \infty} \frac{\partial \overline{u}}{\partial y} = 0$$

To allow for a flexible fitting procedure three parameters with a clear physical meaning are introduced:

$$\overline{u}(y) = a \cdot \mathrm{atan}\big(b \cdot (y - c)\big)$$

Where:

- $a = [m/s]$ scales the velocity magnitude, therefore, when using the whole boundary layer data is proportional to the free-stream velocity.
- $b = [1/m]$ scales with the steepness of the velocity gradient at wall.
- $c = [m]$ can be seen as the wall position predicted by the fit itself.

By fitting this function to the experimental data, the wall shear stress is recovered analytically from the derivative at wall:

$$\left.\frac{\partial \overline{u}}{\partial y}\right|_{w} = ab$$

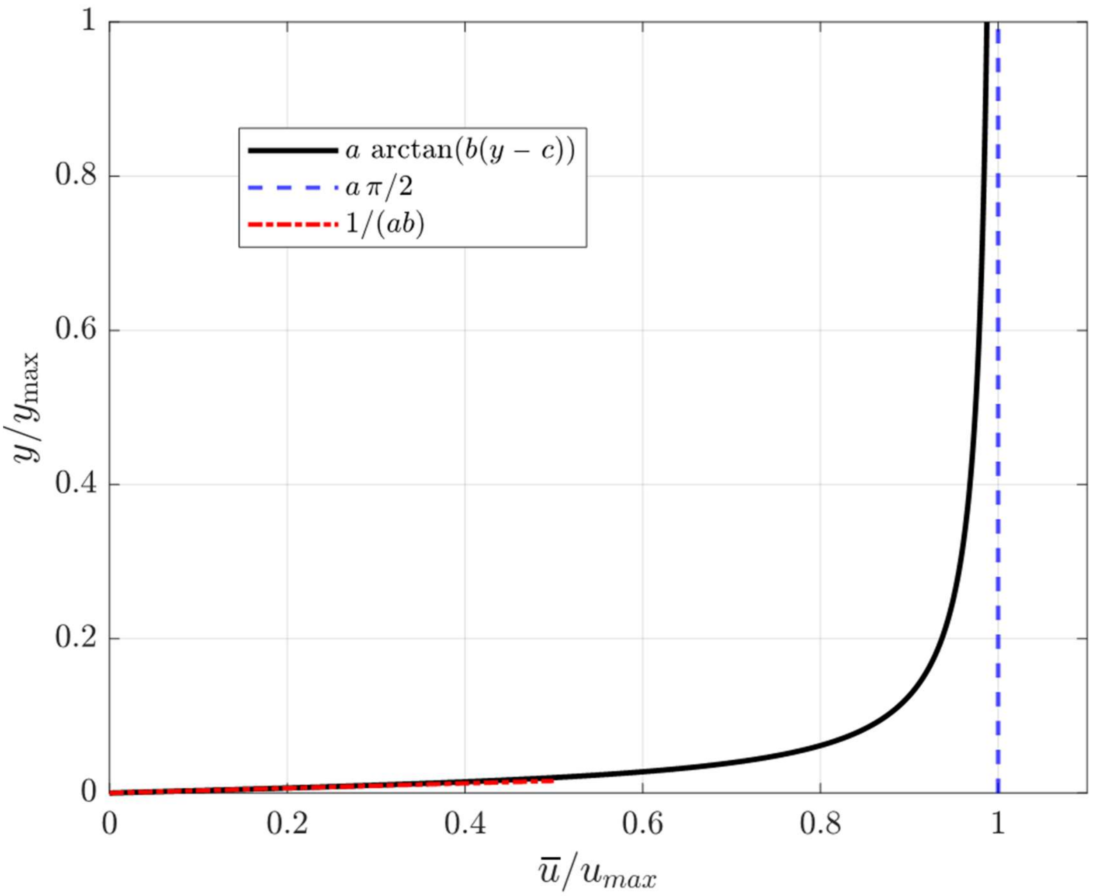

Figure 27 Visual representation of proposed fitting model and influence of fitting parameters $(c = 0)$.

While introducing parameter c means the no-slip condition is no longer enforced at the hypothesized wall location this relaxation is needed to account for experimental constraints and uncertainties in finding the wall position.

CHAPTER VI

Sensitivity analysis and uncertainty assessment

Before applying the proposed model to experimental data, its accuracy and robustness must be verified. This chapter validates the proposed Arctangent against DNS data for a fully developed TBL at similar Re_τ*. Using the synthetic data as a ground truth, the proposed arctangent fit is benchmarked against the classical linear fit addressing three key aspects: sensitivity to fitting domain, robustness to experimental artefacts and experimental cross-validation. Additionally, the Arctangent model is evaluated as an autonomous wall detector on synthetic data. The chapter closes by summarizing the results obtained, highlighting the trade-offs and giving a set of best practices for applying the arctangent model to wall bounded flows.*

6.1 Sensitivity to fitting domain

A sensitivity analysis is performed to assess the robustness of the proposed fitting method with respect to the wall-normal extent of the data used. Neglecting momentarily the spatial resolution limitations inherent to PIV, we first apply the method to the DNS [1] dataset including points starting directly at the wall.

We compare the proposed arctangent model against the standard linear fit by showing the C_f calculated while varying the upper bound of the fitting domain; this way we can highlight for a simplified case the bias error of the analysed method.

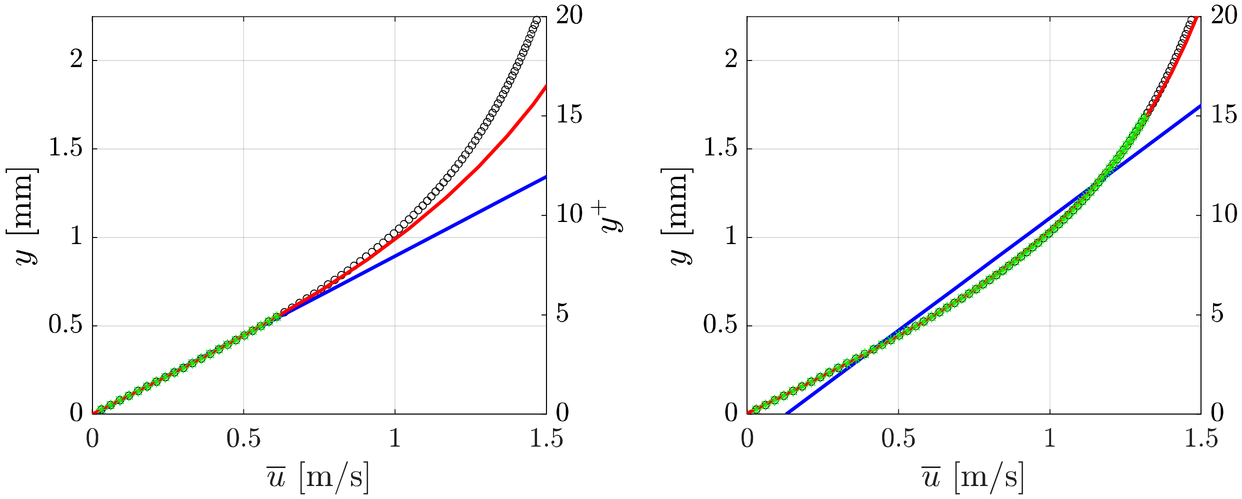

Figure 28 Linear (blue) and Arctangent (red) model with different fitted point (green stars). Left: $y^+ = [0, 5]$. *Right:* $y^+ = [0, 15]$.

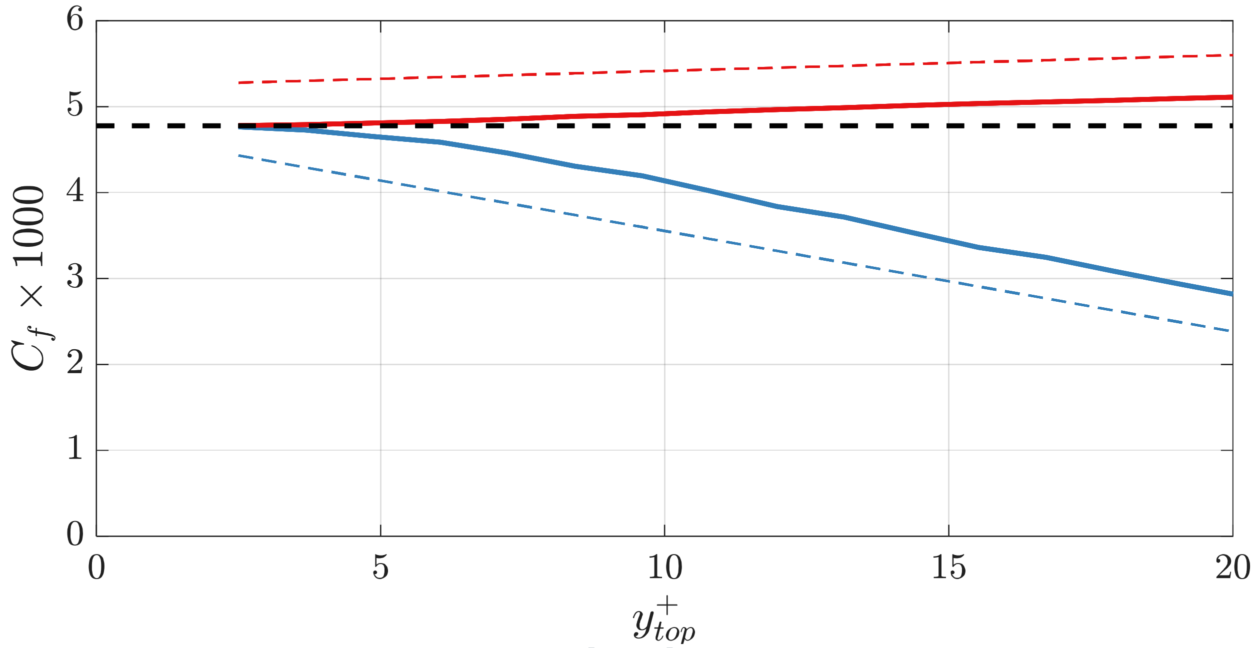

Figure 29 Predicted C_f *as function of fitted points* $y^+_{fit} \in [0, y^+_{top}]$ *for arctangent (solid red) and linear (solid blue) fit. Dashed lines of corresponding colour indicate the bias error sensitivity. Black dashed line represents exact* C_f *from DNS.*

---

[1] The DNS was dimensionalized using integral properties, ensuring that the kinematic viscosity and free-stream velocity match those of our experimental campaign.

As expected, the linear fit degrades rapidly when y^+_{top} exceeds the viscous sublayer yielding a significant negative bias error. Conversely, the arctangent fit exhibits a systematic positive bias error but maintains robustness over a wider domain. The sensitivity to the upper boundary of the fitting domain for the Arctangent model can be approximated to be ≈ 0.3 of the one expressed by the linear model. Additionally, even within the viscous sublayer we can clearly appreciate how the arctangent fit can capture the slight deviations from the linear behaviour.

6.1.1 Lower bound

As previously described in section 4.1.3, PIV presents stark limitations in the near wall region. To prevent the use of measurements affected by low SNR and significant bias errors, it's common practise to avoid the use of velocity vectors corresponding closer to the wall than half an IW size. The robustness of the fitting methods against this data loss is assessed evaluating the relative error for the predicted skin friction coefficient while independently varying the lower (y^+_{bottom}) and upper (y^+_{top}) bounds of the fitting domain.

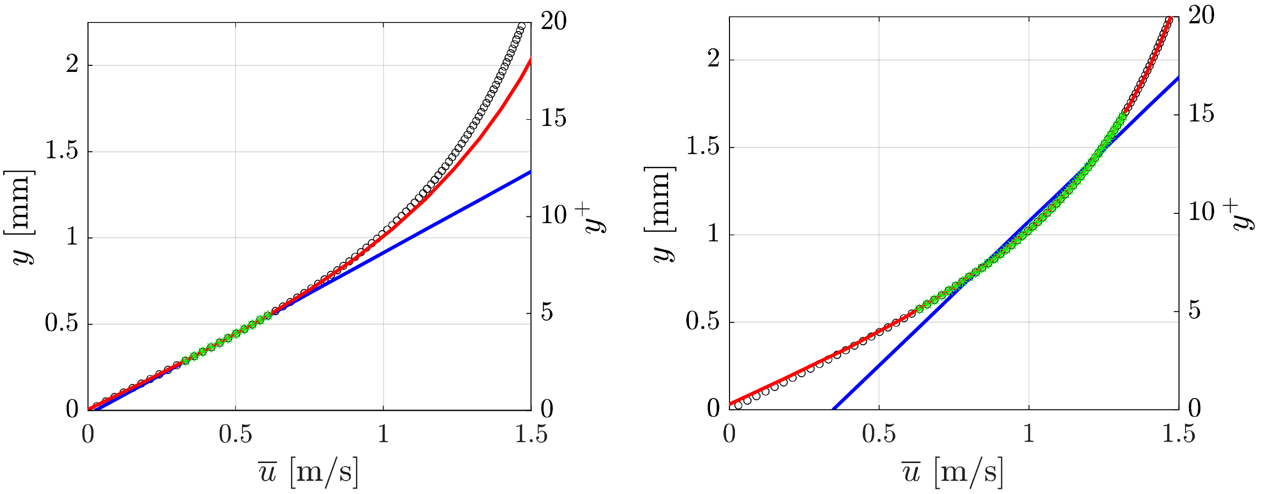

Figure 30 Linear (blue) and Arctangent (red) model behaviour as function of the fitting space. Left: $y^+ = [2.5, 5]$. *Right:* $y^+ = [5,15]$.

Defining an error function as $err = 100 \cdot (C_f^{fit} - C_f^{DNS})/C_f^{DNS}$

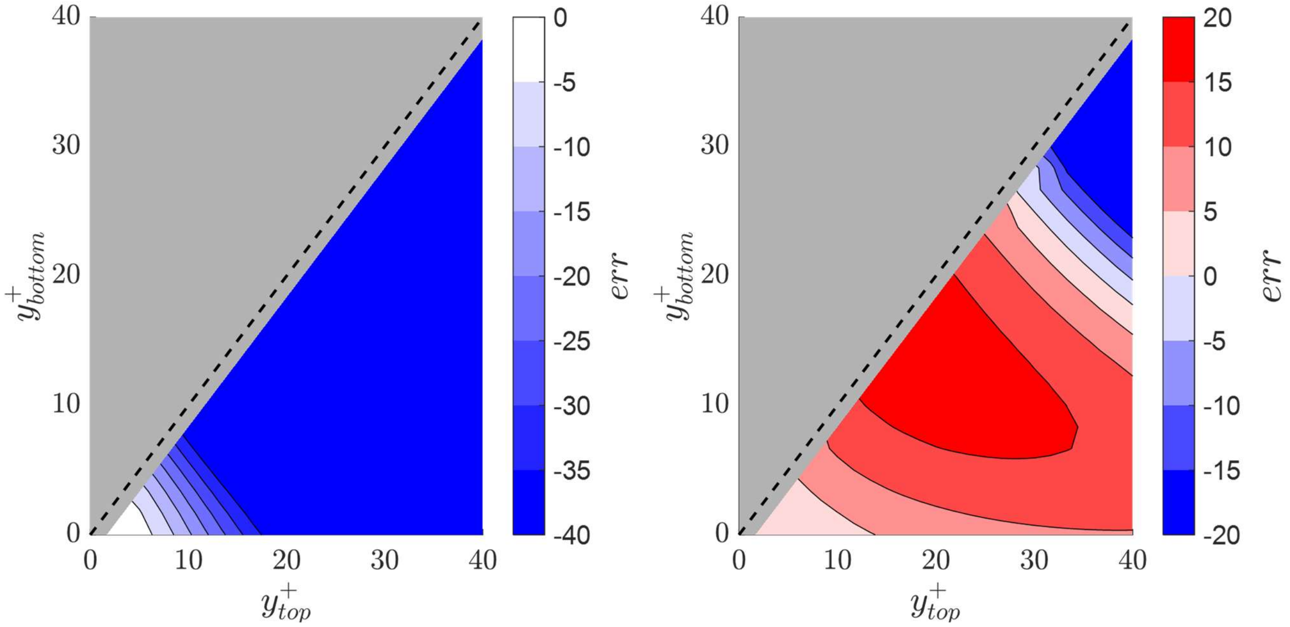

Figure 31 Error as function of the upper and lower boundaries y^+_{top}, y^+_{bottom} *for the different models. Left: linear fit. Right: arctangent fit. Black dashed line is* $y^+_{top} = y^+_{bottom}$.

From Fig.31 it is once again possible to appreciate the opposite bias error that characterises the two methods. In addition, it is easy to appreciate how the region with an error magnitude smaller than 5% is significantly increased reaching upwards of $y^+ \sim 15$ demonstrating a broader useful parametric space.

It is interesting to underline how Fig.31 is, by design, showing the performance of the Arctangent fit for a wider parametric space than the one typically used for skin friction evaluation in cases similar to the one proposed here. This is choice has been made in order to highlight the potential of this model for cases characterized by scarcity measurement points close to the wall (such us 3D measurements, high speed flows…).

6.2 Robustness to measurement noise

Experimental measurements are intrinsically subject to a certain random error and PIV is no exception. In order to evaluate the robustness of the proposed method to such errors as function of the fitting kernel used (i.e. number of points), Gaussian random errors were imposed on the DNS velocity profiles. Following the approach proposed in [33], a Monte Carlo simulation is set-up generating n noisy velocity profiles from the exact DNS data as $u_{noisy} = N(u_{DNS}, \sigma^2)$ where $\sigma = |\varepsilon_{\max}| \cdot |u\_DNS|/3$, ensuring 99.7% of samples remain within $\pm\varepsilon_{MAX}$. For the specific case we selected $\varepsilon_{MAX} = 3$ and $n = 1000$.

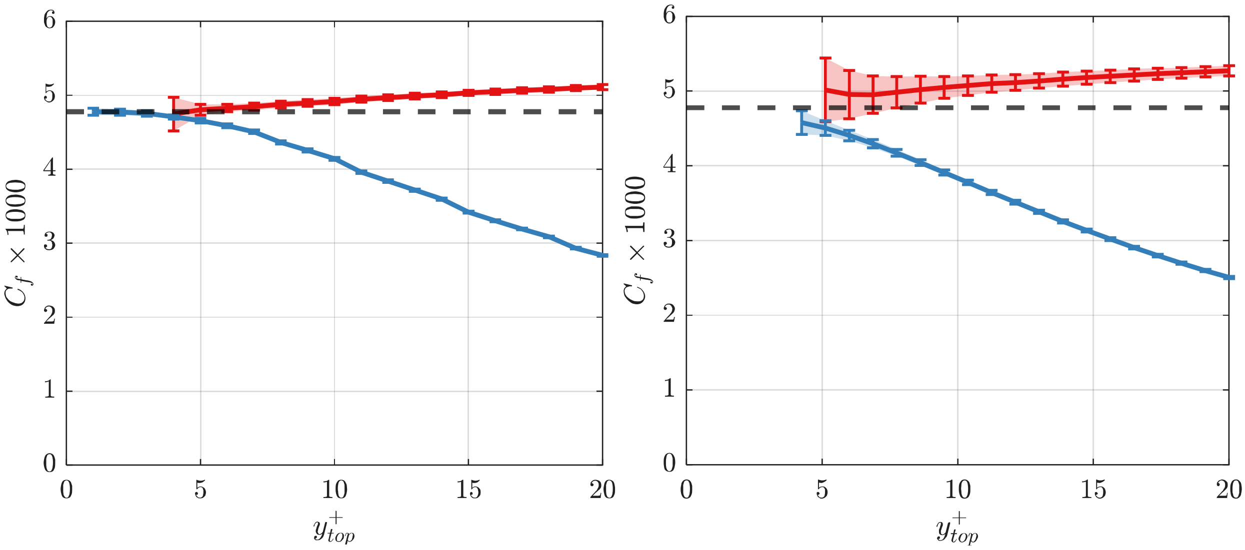

Figure 32 Skin friction coefficient predicted by Linear (blue) and Arctangent (red) model applied on DNS data with superimposed gaussian noise $\varepsilon_{MAX} = 3$. Error bars indicate confidence level of 1σ and black dashed lines represent the exact skin friction coefficient value. Results without enough points do not converge and are not shown. Left: $y^+_{fit} \in [0, y^+_{top}]$. Right: $y^+_{fit} \in [2.5, y^+_{top}]$.

From Fig.32 we can appreciate how, when the number of points available is limited the Arctangent model performs worse that the classic wall slope method; this result is not surprising considering the higher Degrees of Freedom and the correlation between the fitting parameters. Still, increasing y^+_{top} leads to a significant reduction of the std which is shown to be comparable to the Linear fit (used within the viscous sublayer) when $y^+_{upper} \gtrsim 15$.

These results make a strong case for a selection of a higher upper bound of data points used showcasing once again how the drawbacks inherent of the Arctangent model can be offsetted making use of its flexibility.

6.3 Impact of PIV artefacts

The smearing effect described in section 4.1.3 is simulated by applying a moving spatial average filter along the wall normal direction which acts as a simple low pass filter; the change in window size h^+ is strictly related to a change in the number for points used for said filter. The analysis is carried considering $y^+_{bottom} = h^+/2$ and $y^+_{top} = [5\ ,15]$ respectively for the linear and arctangent model.

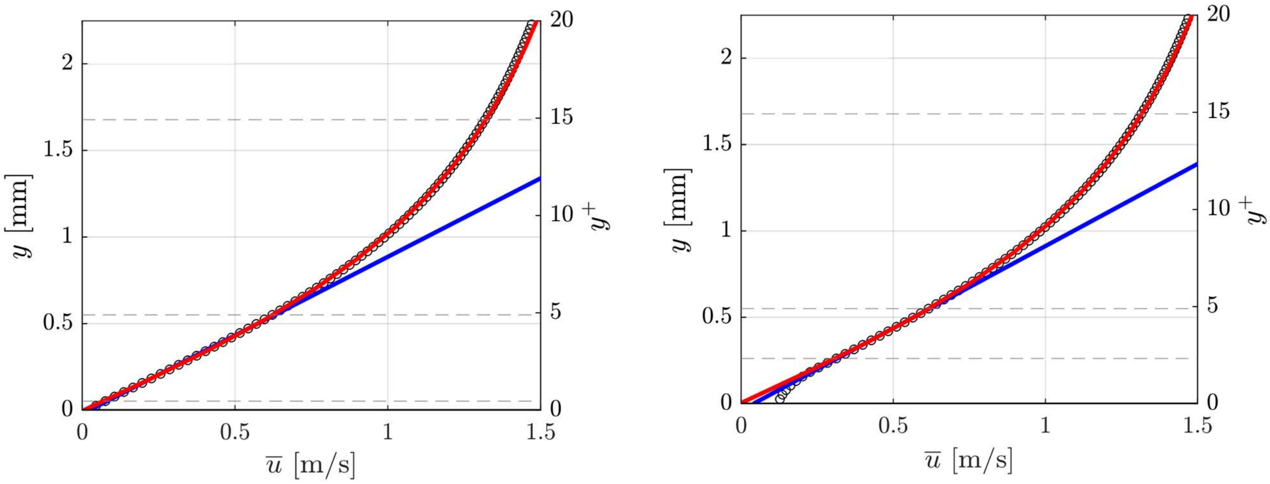

Figure 33 Linear (blue) and Arctangent(red) model behaviour varying filter size; dashed lines represent the fitting boundaries. Left $h^+ = 0$. *Right:* $h^+ = 5$.

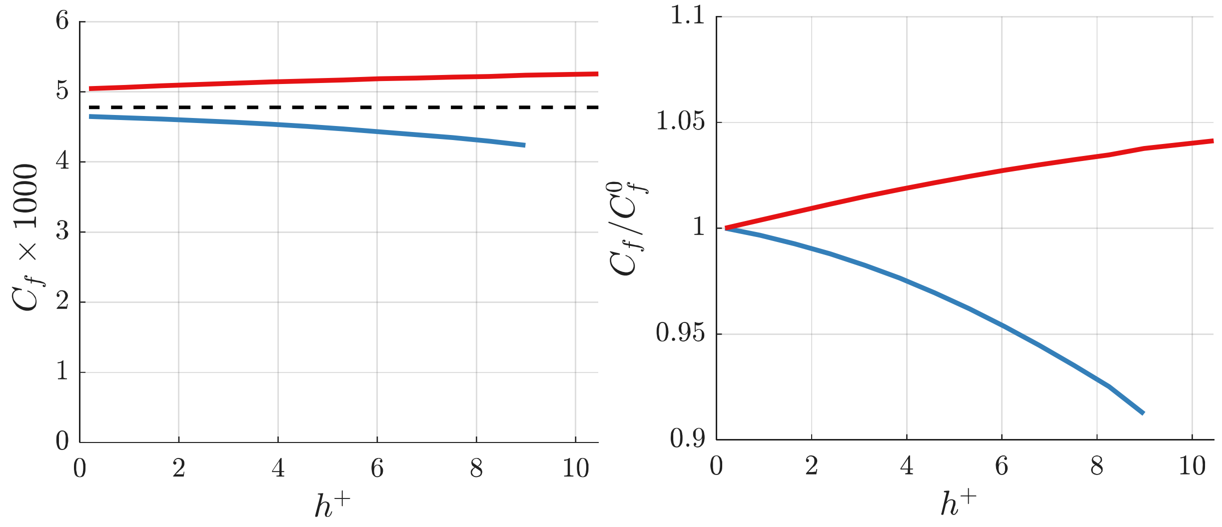

Figure 34 Left: Friction coefficient for Linear (blue)and Arctangent (red) model as function of h^+. *Black dashed line is the exact value of* C_f. *Right: Friction coefficient for arctangent a linear model as function of* h^+ *normalized by the value without filtering.*

As anticipated previously in the error is non null for both linear and arctan fitting even in absence of filtering; more importantly the arctan method is less effected by the a change in window size as we can see in Fig.34 where the skin friction coefficient predicted for different h is normalized with the one equivalent at the absence of the filter. This is once again in line with the idea of an increased robustness of the arctangent fit to the lower boundary of fitting point used.

6.4 Wall position detection

A parallel analysis is performed to assess the accuracy and robustness of the Arctangent model regarding the wall position evaluation.

To simulate a realistic experimental scenario a known spatial shift $\Delta y^+$was applied to the synthetic DNS profiles. The arctangent model was then fitted to the shifted profiles "blindly," restricting the fitting domain to the range $y^+ \in [2.5, 20]$. Fig 35 compares the wall position predicted by the model against the imposed shift in the presence of random gaussian noise (defined as descripted in previous paragraph). The results demonstrate a high degree of accuracy with the method successfully recovering the true wall location with a small bias error $|\Delta y^+ + c^+| < \delta_\nu$. Considering this result in conjunction with the findings from the previous section the arctangent fit is deemed suitable as wall detector in and of itself.

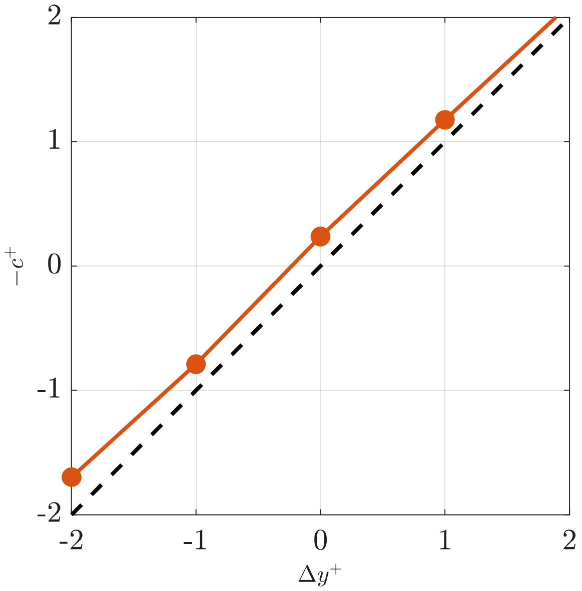

Figure 35 Predicted wall position as function of actual shift (inner units).

6.5 Application to PIV data

To assess the practical feasibility and the coherence with the results obtained from the validation on DNS data the arctangent model is now applied to the PIV data acquired.

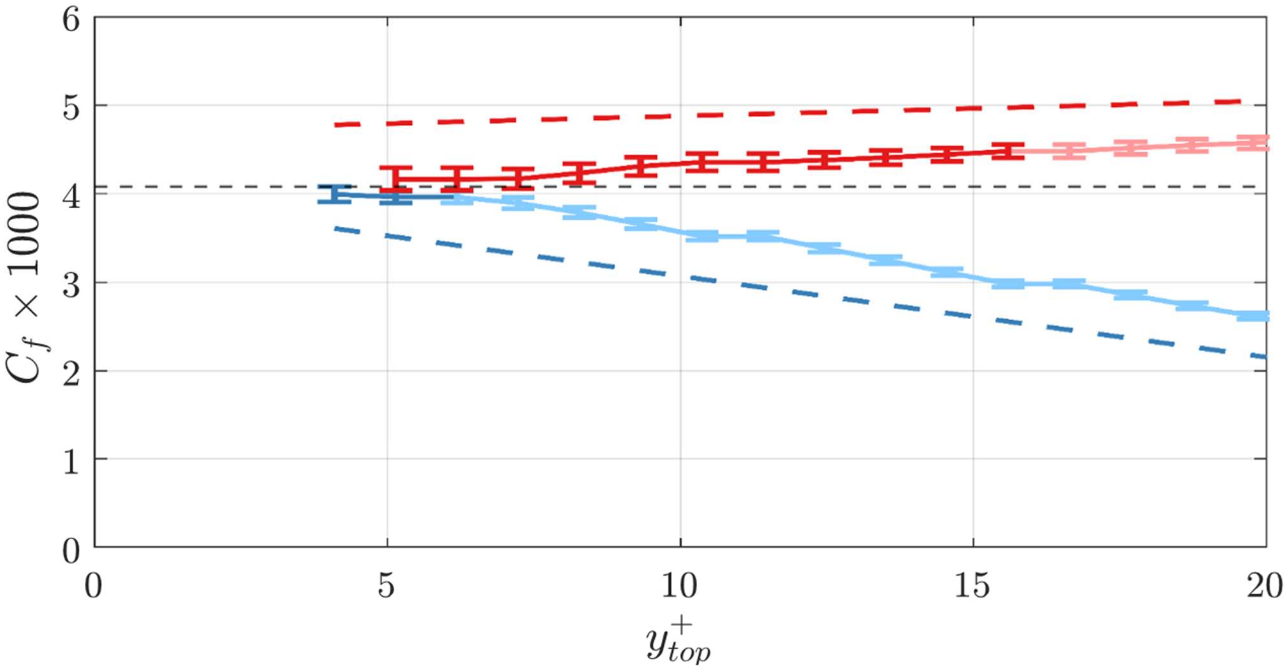

Figure 36 Skin friction coefficient predicted by Arctangent (solid red) and Linear (solid blue) model applied on PIV. Error bars indicate confidence level of 1σ*. Dashed lines of corresponding colour indicate the bias error sensitivity. Black dashed line represents exact* C_f*. Lower boundary set at* $h/2 \approx 2\delta_\nu$.

Fig. 36 confirms the trends observed by the Monte-Carlo analysis on DNS data. As expected, the wall slope method shows a rapid loss in accuracy when increasing the upper boundary of points used while the Arctangent model presents a slight positive bias that remains more stable.

Furthermore, the narrow confidence intervals observed in the valid fitting range indicate high measurement precision, suggesting the random error component of the PIV setup being effectively minimized and validating the quality of the near-wall particle images.

6.6 Summary and best practices

This chapter has presented a sensitivity analysis and validation of the Arctangent model for skin-friction evaluation by benchmarking it against synthetic data and cross-validating the results with our experimental measurements. The main objective of the proposed model was to overcome the inherent limitations of PIV measures for wall-bounded flows, mainly the presence of random measurement noise coupled with a lack of sufficient resolution within the near wall region.

The analysis has led to three significant conclusions regarding the proposed arctangent model; more specifically it was found that the proposed method allows for:

- Expansion of the Valid Parametric Fitting Space:
  The comparative analysis showed the arctangent model to maintain a limited error over a wide domain fitting region while also highlighting a slight positive bias in the reconstruction of the velocity gradient at wall. Quantitatively, if we define a maximum acceptable error of $\varepsilon = \pm 5\%$, the acceptable range of data points for the arctangent fit is more than doubled compared to the linear fit $y^+_{fit} \in [0, 15]$. This extended range is crucial for high Reynolds number flows or setups where near-wall resolution is limited compared to the physical size of the viscous sublayer.

- Mitigation of Measurement Noise effects:
  By extending the available fitting space beyond the linear region, the proposed method allows for a significantly larger sample size effectively compensating for the stability penalty associated with the additional degrees of freedom (parameters) of the arctangent model. If the sensitivity to random error has to be kept equal or smaller than the one expressed by traditional wall slope methods it is suggested to extend the fitting boundary up to $y^+ \approx 15 \div 20$ ideally including 10 or more velocity vectors.

- *In-situ* wall detection:
  Finally, the sensitivity analysis regarding the wall-normal coordinate confirmed that the arctangent model can accurately identify the wall position. This allows the method to act as a virtual wall detector using only information present inside the flow field without having to rely on external knowledge or presence of reflections. Although the model exhibits a small positive of bias the error remains bounded $\pm 1\delta_\nu$.

In summary the arctangent fit offers a superior practical compromise for experimental measurements. It trades a negligible systematic bias for a substantially reduced sensitivity to the fitting domain while maintaining similar robustness against measurement noise.

In the context of the experimental campaign presented in the thesis, the described bias would apply for both the uncontrolled and controlled case; supposing the error to be consistent across the two cases, for the purpose of investigating relative differences instead of absolute values of the skin friction coefficient, the net effect is negligible.

CHAPTER VII

Experimental set-up and data processing

The experimental methodology described in the current chapter was designed to address the constraints of high spatial resolution and extended domain previously described. This chapter details the experimental facility, the actuation hardware of the spanwise forcing mechanism and the PIV acquisition system. Additionally, the digital image processing workflow is outlined, from pre-processing to the specific parameters and algorithms used for PIV and post-processing.

7.1 Wind tunnel and Forcing mechanism

The experimental campaign was carried out in the W-tunnel, a low-speed open-return wind tunnel located in the High-Speed Laboratory of Delft University of Technology. The tunnel is equipped with a $9:1$ contraction, which leads to a square exit section of $40 \times 40\ cm$. Within this specific setup the free-stream velocity can be set between 2 and $35\ m/s$; for the present investigation the free stream velocity was set at 3.5 m/s corresponding to a free stream turbulence intensity below 1%.

Downstream of the contraction cone, the flow enters a wooden rectangular section housing a flat plate of length $0.9\ m$ with an elliptical leading edge positioned $0.10\ m$ above the bottom wall. A turbulent boundary layer developing under ZPG condition is obtained by forcing the transition with an array of $1\ cm$ cubic elements spaced by $2\ cm$ and placed a few centimetres downstream of the leading edge [10].

The wooden section transitions into the actual plexiglass test section which ensures full optical access for flow illumination and imaging. In this section the flat plate is divided in three segments: a fixed upstream section needed to study the reference flow, a central oscillating plate and a fixed section downstream, needed to study the recovery transient. The measured section extends from 8 cm upstream the L.E. to $\approx 20\ cm$ downstream the T.E. of the oscillating plate leaving $\approx 2\delta$ before the last part of the flat plate.

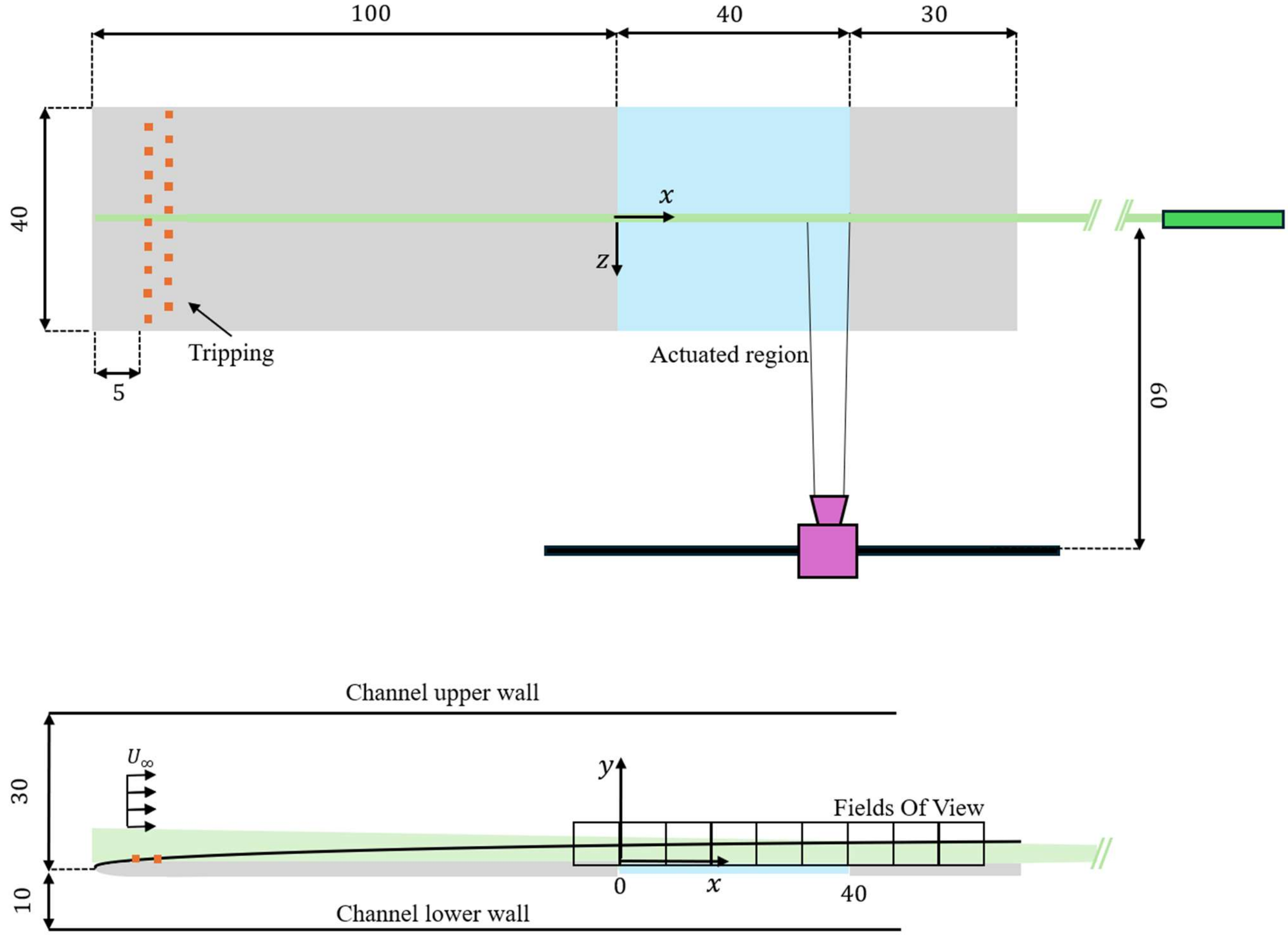

Figure 37 Schematic of the experimental set-up to scale $[cm]$ *Top: Top-down view. Bottom: side view.*

The oscillating plate, situated $\approx 1\ m$ downstream of the tripping devices, has a length of $0.4\ m$ ($\approx 10\delta$) was driven by a crank-slider mechanism powered by a Maxon brushless DC motor and operated through a MIP100 controller. This mechanical system allowed for harmonic oscillations of frequencies up to $20\ Hz$ ($T^+ \approx 100$) with a peak-to-peak displacement of $4\ cm$ resulting in a maximum velocity $W_m \approx 2.5\ m/s$ ($W_m^+ \approx 7$).

Small interface gaps of $\approx 0.2\ mm$ (around two viscous units) are present between the moving segment and the adjacent fixed sections. A thin wooden plate has been installed below the oscillating section to prevent fluid ejections due to high pressure stagnation points caused by thickness discontinuities between oscillating and fixed sections.

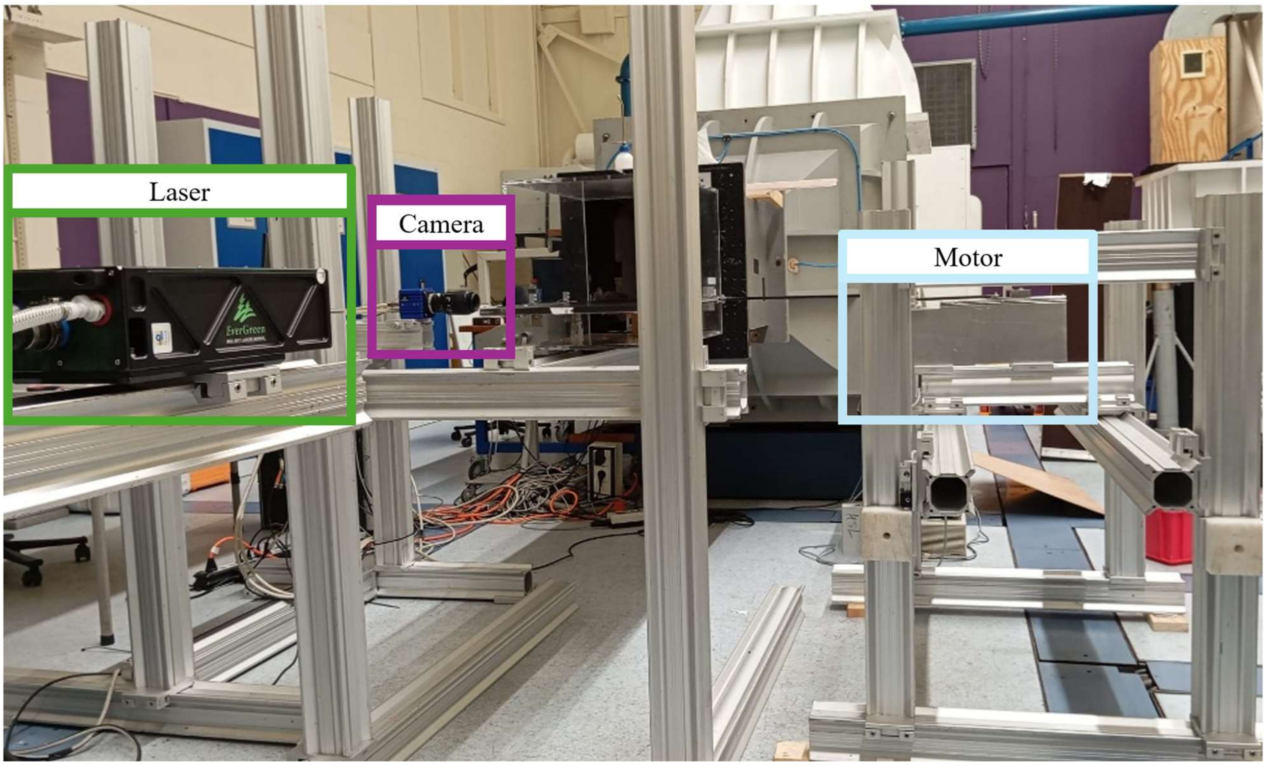

Figure 38 Photo of the experimental set-up; highlight on the different components.

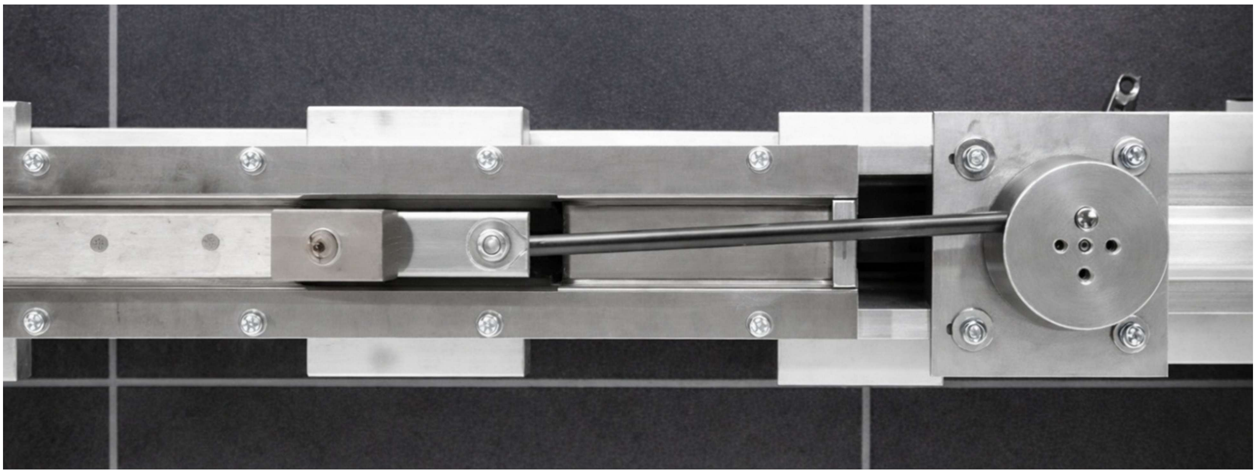

Figure 39 Crank slider mechanism, top down view.

7.2 PIV setup and parameters

The PIV measurements were conducted using a single LaVision Imager CMOS camera fitted with Nikkor lenses. The camera has been fixed to moving platform atop of a streamwise oriented rail at $\approx 60\ cm$ from the target plane resulting in a FOV of $\approx 8\ cm$. Measurements have been acquired at nine distinct streamwise stations in order to cover the whole region affected by the wall forcing even accounting for a small overlap ($\lesssim 1\ cm$).

Category	Parameter	Value	Unit
Seeding	Seeding type	Fog	–
	Particle size	1	μm
	Particles/pixel	0.33	–
	Stokes' Number	$\sim 10^{-3}$	–
Illumination	Laser type	Nd:YAG	–
	Energy	2×200	mJ
	Max pulse repetition	15	Hz
	Mode of operation	Q-switched	–
	Laser width	1.5	mm
Imaging	Sensor type	sCMOS	–
	Sensor size	2560 x 2160	px
	Pixel pitch	6.5	μm
	Focal length	105	mm
	$f_{\#}$	8	–
	Magnification	0.2	–
Recording	N. snapshot	1000	–
	Pixel size	30	px/mm
	Δt	150	μs
	Freestream particle displacement	17	px
	Acquisition frequency	7	Hz

Table 2 PIV setup parameters.

Flow visualization was facilitated by seeding the air with fog droplets of diameter $d_p = 1\mu m$, generated using a SAFEX smoke generator. To allow for a homogeneous distribution of seeding the smoke was left circulating along the wind tunnel laboratory, until the desired concentration was reached.

Illumination was achieved via a Quantel Evergreen 200 Nd:YAG laser system, delivering two pulses of $200\ mJ$ at a frequency of $15\ Hz$; the laser was fitted with a set of cylindrical lenses that shaped a $1.5\ mm$ thick wall normal laser sheet which was aligned parallel to the flow direction and positioned at the mid-plane along the streamwise reference axis.

Precise synchronization between the laser, cameras, and image acquisition system was maintained using a LaVision Programmable Timing Unit, operated through DaVis 10.2 software.

In order to minimize loss of correlation by out-of-plane (spanwise) tracers' motion, the pulse separation was limited to ensure a maximum spanwise displacement lower than a quarter of the laser sheet thickness. In doing so it was assumed the tracers in the near wall region to convect at the same speed of the oscillating wall therefore adopting the peak wall velocity as a conservative estimate.

The frequency of acquisition was chosen to result in a temporal separation of approximately 10 times the characteristic boundary layer turnover time of ($\Delta t \geq \delta / U_\infty$) as to guarantee decorrelation of the images.

7.3 Data processing

Data processing was performed via a hybrid workflow utilizing both the LAVISION DAVIS 10.2 software suite for PIV calculation and custom MATLAB scripts for pre-processing alignment and post-processing analysis.

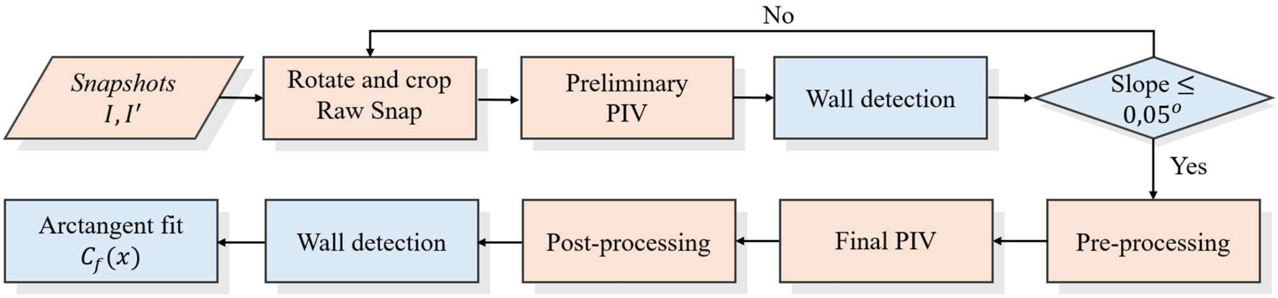

Figure 40 Flowchart for investigation of skin friction coefficient distribution. Ligh blue: MATLAB. Pink: DAVIS.

To account for minor camera misalignments the images where digitally rotated to align the wall with the horizontal axis of the Cartesian grid. This process was performed iteratively with an initial rotation based on visual inspection that was then refined by performing a preliminary PIV analysis on a snapshot's subset. The rotation of the original images was repeated until a slope of $< 0.05^o$ was achieved.

Image preprocessing consisted in a normalization of the instantaneous intensity field with the rescaled (close to unity) averaged intensity field in order to deal with steady reflections followed by a minimum intensity background subtraction on a kernel of 7 snapshots to reduce unsteady reflections and allow for a better recognition of tracing particles.

After the PIV was performed with the parameters described in Tab.3 spurious vectors were detected and replaced using a three-pass median filter based the Universal Outlier Detection criterion.

Processing	Multi-pass processing with iterative window deformation		
	First interrogation window	96 x 96	px
	Final interrogation window	32 x 8	px
	Overlap	75	%
	Vector spacing (wall normal)	132	μm
		~ 1.5	δ_ν
	Dynamic Spatial Range	320	–

Table 3 PIV processing parameters for skin friction analysis.

When defining the fitting space for the determination of C_f the boundaries have been kept constant within each FOV but adjusted across them to account for the natural growth of the boundary layer and slight misalignments of the plate. The same procedure has been used for the wall position in order to account for different cropping across different data sets. Finally, to highlight the streamwise trends, a spatial median filter was applied to the resulting skin friction coefficient distribution in order to further reduce high-frequency spatial noise.

CHAPTER VIII

Results

In this chapter the findings of the experimental campaign are presented. A first section is used for the characterization of the unactuated flow in order to validate flow and measurement quality against literature data. Subsequently the analysis shifts to the streamwise evolution of skin-friction coefficient across the oscillating plate focusing on the magnitude of Drag Reduction achieved as well as its modelling comparing results with literature findings.

8.1 Boundary layer characterization

The baseline (uncontrolled) TBL is characterized and compared against DNS data at a comparable Re_τ.

$U_\infty\ [m/s]$	$\delta\ [mm]$	$\delta^*\ [mm]$	$\theta\ [mm]$	H	$\delta_\nu\ [\mu m]$	$u_{\tau,0}\ [m/s]$	Re_τ	Re_θ
3.5	41	5.9	4.2	1.4	89	0.17	470	970

Table 4 Reference Boundary Layer characterization.

The measured skin friction coefficient $\left(C_f \approx 4.6 \cdot 10^{-3}\right)$ is approximately 9% higher than the one predicted by the Coles-Fernholz relation for the measured Re_θ. This deviation could be explained by the strong tripping and the previously discussed bias error associated with the arctangent model.

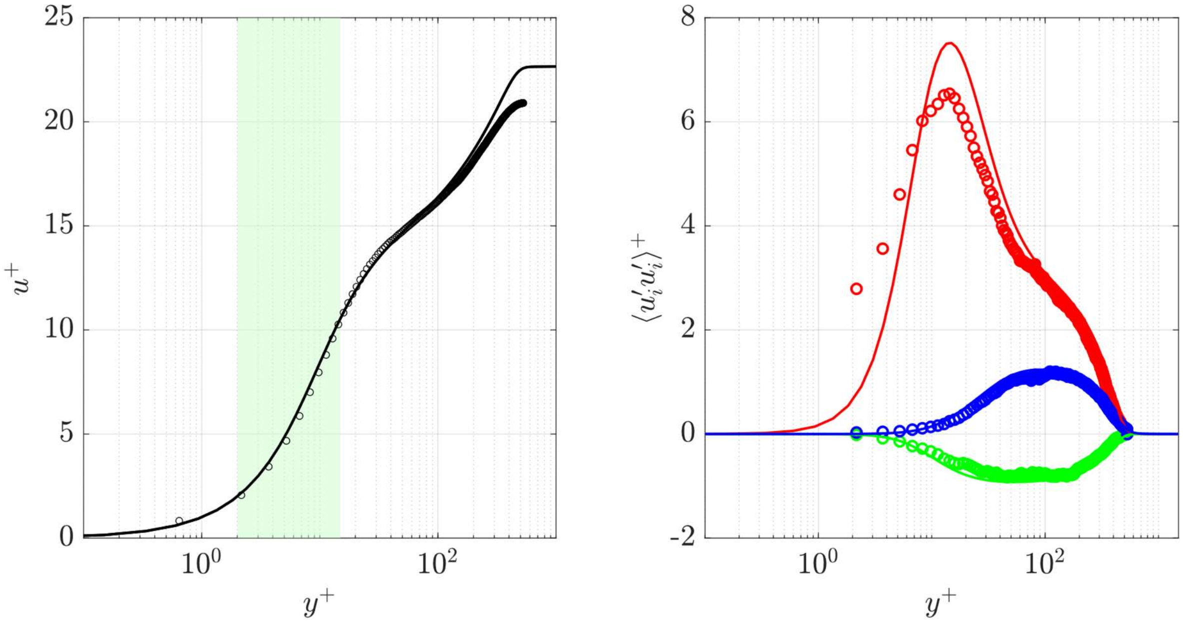

Figure 41 Left: Normalized mean velocity profile for the uncontrolled case; light green show fitting points used. Right: Normalized Reynolds stresses profiles for the uncontrolled case. Circles: experimental data. Data from Schlatter and Örlü.

From Fig 38. we can appreciate a good level of coherence between experimental data and literature results within the inner layer down to $y^+ \approx 2$ vouching for an accurate direct wall shear stress measurement.

From the second graph normal streamwise shear stress $\langle u'u' \rangle^+$ exhibits the usual peak at $y^+ \approx 15$, consistent with the expected behaviour. In the near-wall region ($y^+ \lesssim 6$) the results do not align; this is expected considering the larger IW used for the analysis [1] and higher sensitivity of second order statistics to an environment characterized with lower SNR.

A slight underprediction of the peak value of all Reynolds stresses is observed when compared to the reference data; this is likely due to the previously described spatial averaging effects of PIV and bias error intrinsic of the Atan model which was used to evaluate $u_{\tau,0}$.

---

[1] Final pass IWs where not stretched in the streamwise direction.

8.2 Skin friction coefficient evolution

The streamwise evolution of the skin friction coefficient is reconstructed applying the workflow described in section 7.3 And compositing the result of the different FOV merging the overlapping regions that were present by design.

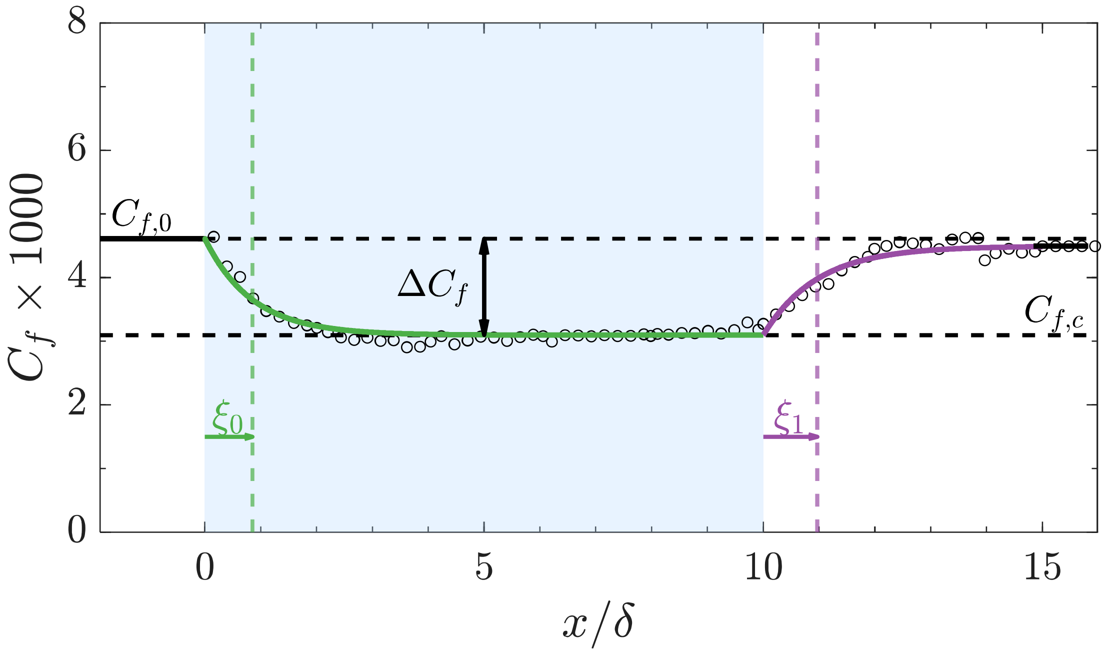

Figure 42 Spatial evolution of skin friction coefficient across the oscillating section (light blue). Black circles represent the experimental measurements (down sampled for clarity). Solid lines represent the fitted model: onset (green) and offset (purple).

From Fig. 39 we can clearly appreciate the variation in skin friction coefficient induced by wall forcing with the flow rapidly evolving from the reference to the controlled state and back across the oscillating plate. Additionally, it is possible to appreciate a good alignment with the proposed exponential fit described in section 3.2.3.

Notably the achieved drag reduction is calculated to be $\approx 30\%$; this result exceeds the theorical prediction derived by Quadrio's map for our actuation parameter. In spite of this higher level of DR measured, looking at the energy budget, as anticipated in previous chapters, a significant deficit is highlighted. When comparing aerodynamic power savings ($P_{saved} = \Delta D \cdot U_\infty$) to the power consumed by the actuator ($P_{act} = V \cdot I$) the resulting efficiency is close to zero with the power required being orders of magnitude higher than the savings:

$$\frac{P_{saved}}{P_{act}} = \frac{(DR \cdot D_0)\, U_\infty}{(\Delta V \cdot I)_{act}} \sim 10^{-5}$$

Finally, looking at the duration of the spatial transients, Fig. 39 show the characteristic measured length scale to be similar for both the onset and offset $\xi_0, \xi_1 \approx \delta$. While this result is consistent with the trends shown in literature for the first transient, such a persistence of the effect is in contrast with previous datasets.

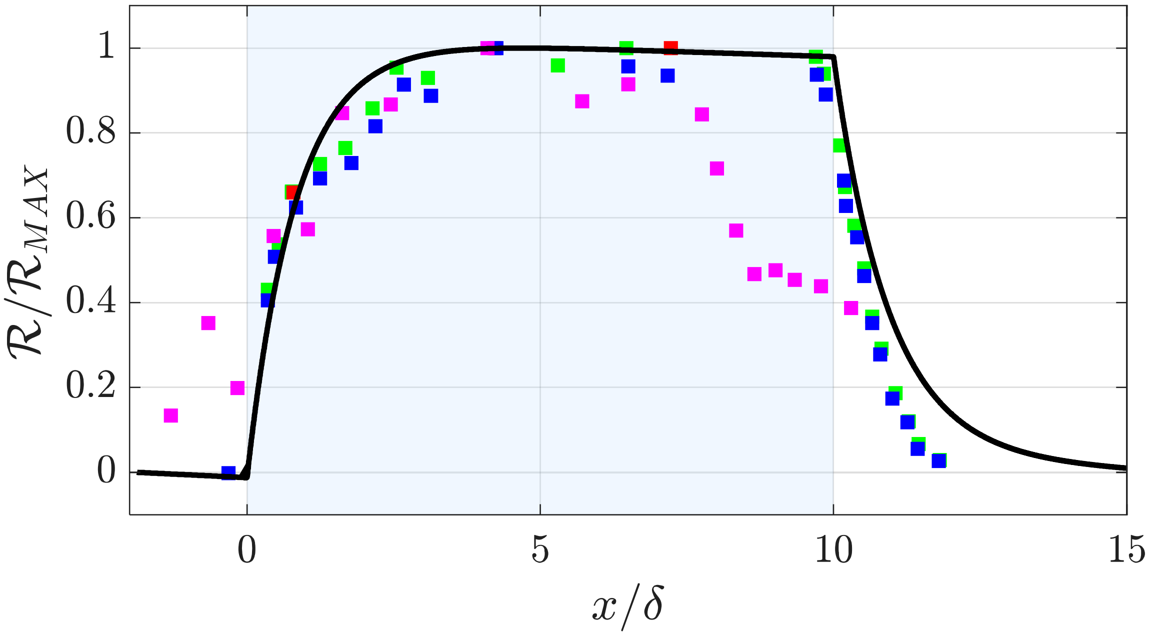

Figure 43 Normalized drag reduction modelled (continuous line) compared with results from other experimental campaigns (squares). Data from: green– Wu et al; red – Trujillo et. Al; blue – Bogart et. Al; magenta – Choi.

CHAPTER IX

Conclusions

The work presented in this thesis developed and validated a robust experimental methodology to estimate the spatial evolution of skin-friction coefficient from planar PIV in the context of turbulent Drag Reduction via spanwise wall oscillations. The main contribution is the adaptation and thorough validation of a non-linear Arctangent-based model used for reconstructing the near-wall mean velocity profile in order to recover wall shear stress from noisy, resolution-limited PIV data. In the following chapter a summary of the main results and recommendations for future work are summarized.

9.1 Metrology

The arctangent fitting function was originally proposed as a viable option to surpass resolution limitations in 3D measurements around complex geometry [34]. In the present work, this formulation is not introduced as a new model, but rather validated and extended for less extreme cases in which the relaxation of the constraints on the fitting domain can still be beneficial.

Validation against high-fidelity DNS and against our experimental dataset demonstrates that the arctangent model substantially expands the usable fitting region when compared with the classical linear fit. Quantitatively, for a maximum acceptable error of $\approx 5\%$ the arctangent fit allows for the upper fitting bounds to extend well beyond the viscous sublayer up to $y^+ \sim 15$ increasing the number of available points and reducing statistical uncertainty. Monte Carlo simulations show the larger fitting kernel to compensate for the model's additional Degrees Of Freedom. If the fitting boundary is extended up to $y^+ \gtrsim 15$ the arctangent model yields comparable variance to the linear approach while only introducing a small positive bias.

An additional advantage is that the arctangent fit can infer the wall position as a free fitting parameter, acting as an implicit wall detector when other methods are unavailable. Sensitivity studies indicate that wall-position errors, interrogation-window smearing and quantization effects have limited impact on the recovered τ_w when the arctangent model is used within the recommended fitting boundaries.

As discussed in this work, the arctangent formulation introduces additional Degrees Of Freedom compared to classic wall slope strategies; in cases where the wall position is known with high accuracy, this limitation could be mitigated by re-introducing a physics-informed constraint enforcing the no-slip condition. Doing so the fitting parameter c will be null reducing the fitting problem to:

$$u = a \cdot \arctan(b \cdot y)$$

Preliminary tests indicate this constrained formulation to provide improved accuracy in the estimation of wall shear stress and robustness to random noise at the expense of a significantly increased sensitivity with respect to wall-position uncertainty. An assessment of this trade-off represents a natural extension of the present study.

Finally, the present framework is not limited to the arctangent function. Any fitting function satisfying the requirements identified in section 5.2.1, namely monotonicity, near-wall regularity, and boundedness, could be investigated within the same validation process. Exploring alternative functional forms may further improve accuracy while retaining the practical advantages demonstrated here.

9.2 Spanwise wall forcing

The uncontrolled boundary layer has been validated against DNS data at similar friction Reynolds, showing a good agreement when taking into account the overestimation of the friction velocity derived by the use of the Arctangent model.

Spanwise wall forcing has been applied with the following parameters $T^+ \approx 100$, $W_m^+ \approx 7$. Direct wall shear stress evaluation, enabled by the newly developed methodology, showed an estimated drag-reduction level of $\sim 30\%$ consistent with previous literature data, albeit with a modest overestimation when compared to Quadrio’s map. Crucially the power required for actuation exceeds the viscous drag saving by many orders of magnitude reaffirming the need for a development of passive flow control techniques.

The full spatial evolution of the mean skin-friction coefficient has been presented showing a good agreement of the spatial transients with the proposed exponential response model. Notably, both transients display a characteristic length scale of $\xi \approx \delta$ implying a duration of the transients of $\sim 5\delta$; while the onset length agrees with previous reports, the persistence of the recovery transient found here is unusually long. Despite the nominal duration of the transient previously described, due to the functional form of the adaptation of the skin friction, the region in which the DR is appreciable is much more limited with $\sim 90\%$ of the relaxation happening within $\sim 2\xi$.

Future research could focus on shedding light on the main physical mechanism behind Drag Reduction. Now being able to evaluate the continuous evolution of skin-friction across the oscillating plate one could relate it to the spatial regeneration length scale of the coherent structures present in a TBL and diffusion of the Stokes layer. At the same time, experimental evaluation of high Drag Reduction regimes by spanwise wall forcing remains scarce; extending the investigation to different actuation parameters could further validate the universality of the proposed response model.

Bibliography

[1] M. Klöwer, M. R. Allen, D. S. Lee, S. R. Proud, L. Gallagher, and A. Skowron, “Quantifying aviation’s contribution to global warming,” *Environ. Res. Lett.*, vol. 16, no. 10, p. 104027, Oct. 2021, doi: 10.1088/1748-9326/ac286e.

[2] H. Ritchie, “What share of global CO_2 emissions come from aviation?” 2024. Accessed: Jan. 30, 2026. [Online]. Available: https://archive.ourworldindata.org/20251125-173858/global-aviation-emissions.html

[3] A. H. Epstein, “Aeropropulsion for Commercial Aviation in the Twenty-First Century and Research Directions Needed,” *AIAA J.*, vol. 52, no. 5, pp. 901–911, May 2014, doi: 10.2514/1.J052713.

[4] N. G. Ningappa, K. Vishweswariah, S. Ahmed, M. D. Bouguern, M. R. Anil Kumar, and K. Zaghib, “Sustainable propulsion and advanced energy-storage systems for net-zero aviation,” *Energy Environ. Sci.*, vol. 18, no. 22, pp. 9786–9838, 2025, doi: 10.1039/D5EE02865E.

[5] A. Abbas *et al.*, “Drag reduction via turbulent boundary layer flow control,” *Sci. China Technol. Sci.*, vol. 60, no. 9, pp. 1281–1290, Sep. 2017, doi: 10.1007/s11431-016-9013-6.

[6] K.-S. Choi, J.-R. DeBisschop, and B. R. Clayton, “Turbulent Boundary-Layer Control by Means of Spanwise-Wall Oscillation,” *AIAA J.*, vol. 36, no. 7, pp. 1157–1163, Jul. 1998, doi: 10.2514/2.526.

[7] G. Cafiero, E. Amico, and G. Iuso, “Manipulation of a turbulent boundary layer using sinusoidal riblets,” *J. Fluid Mech.*, vol. 984, p. A59, Apr. 2024, doi: 10.1017/jfm.2024.256.

[8] P. Ricco, M. Skote, and M. A. Leschziner, “A review of turbulent skin-friction drag reduction by near-wall transverse forcing,” *Prog. Aerosp. Sci.*, vol. 123, p. 100713, May 2021, doi: 10.1016/j.paerosci.2021.100713.

[9] AirShaper, “What is a boundary layer? Laminar and turbulent boundary layers explained.” Accessed: Jan. 30, 2026. [Online]. Available: https://airshaper.com/videos/what-is-a-boundary-layer-laminar-and-turbulent-boundary-layers-explained/TwOxa9rAOfE

[10] K. U. Kempaiah, "Active control of turbulent skin-friction: an experimental study," Ph.D. dissertation, Dept. of Aerospace Engineering, Delft Univ. of Technology, Delft, The Netherlands, Nov. 2023.

[11] A. Towne *et al.*, “A Database for Reduced-Complexity Modeling of Fluid Flows,” Jun. 23, 2022, *arXiv*: arXiv:2206.11801. doi: 10.48550/arXiv.2206.11801.

[12] P. Schlatter and R. Örlü, “Assessment of direct numerical simulation data of turbulent boundary layers,” *J. Fluid Mech.*, vol. 659, pp. 116–126, Sep. 2010, doi: 10.1017/S0022112010003113.

[13] W. Schoppa and F. Hussain, “Coherent structure generation in near-wall turbulence,” *J. Fluid Mech.*, vol. 453, pp. 57–108, Feb. 2002, doi: 10.1017/S002211200100667X.

[14] G. Gómez de Segura, "Turbulent drag reduction by anisotropic permeable substrates," Ph.D. dissertation, Dept. of Engineering, Univ. of Cambridge, Cambridge, UK, Apr. 2019.

[15] W. Schoppa and F. Hussain, “Coherent structure generation in near-wall turbulence,” *J. Fluid Mech.*, vol. 453, pp. 57–108, Feb. 2002, doi: 10.1017/S002211200100667X.

[16] L. Zhang, X. Shan, and T. Xie, “Active Control for Wall Drag Reduction: Methods, Mechanisms and Performance,” *IEEE Access*, vol. 8, pp. 7039–7057, 2020, doi: 10.1109/ACCESS.2020.2963843.

[17] R. J. Adrian, “Hairpin vortex organization in wall turbulence,” *Phys. Fluids*, vol. 19, no. 4, p. 041301, Apr. 2007, doi: 10.1063/1.2717527.

[18] F. Gattere, A. Chiarini, and M. Quadrio, “Dimples for Skin-Friction Drag Reduction: Status and Perspectives,” *Fluids*, vol. 7, no. 7, p. 240, Jul. 2022, doi: 10.3390/fluids7070240.

[19] S. Chernyshenko, “Drag reduction by a solid wall emulating spanwise oscillations. Part 1,” Apr. 16, 2013, *arXiv*: arXiv:1304.4638. doi: 10.48550/arXiv.1304.4638.

[20] R. García-Mayoral and J. Jiménez, “Drag reduction by riblets,” *Philos. Trans. R. Soc. Math. Phys. Eng. Sci.*, vol. 369, no. 1940, pp. 1412–1427, Apr. 2011, doi: 10.1098/rsta.2010.0359.

[21] B. S. Sidhu, M. R. Saad, K. Z. K. Ahmad, and A. C. Idris, “RIBLETS FOR AIRFOIL DRAG REDUCTION IN SUBSONIC FLOW,” vol. 11, no. 12, 2016.

[22] K. Koch, B. Bhushan, and W. Barthlott, “Multifunctional surface structures of plants: An inspiration for biomimetics,” *Prog. Mater. Sci.*, vol. 54, no. 2, pp. 137–178, Feb. 2009, doi: 10.1016/j.pmatsci.2008.07.003.

[23] P. R. Spalart and J. D. McLean, “Drag reduction: enticing turbulence, and then an industry,” *Philos. Trans. R. Soc. Math. Phys. Eng. Sci.*, vol. 369, no. 1940, pp. 1556–1569, Apr. 2011, doi: 10.1098/rsta.2010.0369.

[24] M. Skote, “Turbulent boundary layer flow subject to streamwise oscillation of spanwise wall-velocity,” *Phys. Fluids*, vol. 23, no. 8, p. 081703, Aug. 2011, doi: 10.1063/1.3626028.

[25] M. Quadrio and P. Ricco, “Critical assessment of turbulent drag reduction through spanwise wall oscillations,” *J. Fluid Mech.*, vol. 521, pp. 251–271, Dec. 2004, doi: 10.1017/S0022112004001855.

[26] M. Skote, M. Mishra, and Y. Wu, “Wall Oscillation Induced Drag Reduction Zone in a Turbulent Boundary Layer,” *Flow Turbul. Combust.*, vol. 102, no. 3, pp. 641–666, Mar. 2019, doi: 10.1007/s10494-018-9979-2.

[27] P. Ricco and S. Wu, “On the effects of lateral wall oscillations on a turbulent boundary layer,” *Exp. Therm. Fluid Sci.*, vol. 29, no. 1, pp. 41–52, Dec. 2004, doi: 10.1016/j.expthermflusci.2004.01.010.

[28] M. Galli, N. Scaiola, F. F. J. Schrijer, and F. Scarano, “Spatial evolution of drag reduction across a finite oscillating wall”. Under revision.

[29] M. Raffel, C. E. Willert, F. Scarano, C. J. Kähler, S. T. Wereley, and J. Kompenhans, *Particle Image Velocimetry: A Practical Guide*. Cham: Springer International Publishing, 2018. doi: 10.1007/978-3-319-68852-7.

[30] N. A. Buchmann, C. E. Willert, and J. Soria, “Pulsed, high-power LED illumination for tomographic particle image velocimetry,” *Exp. Fluids*, vol. 53, no. 5, pp. 1545–1560, Nov. 2012, doi: 10.1007/s00348-012-1374-5.

[31] M. D. Atkins, “Chapter 5 - Velocity Field Measurement Using Particle Image Velocimetry (PIV)”.

[32] C. J. Kähler, S. Scharnowski, and C. Cierpka, “On the resolution limit of digital particle image velocimetry,” *Exp. Fluids*, vol. 52, no. 6, pp. 1629–1639, Jun. 2012, doi: 10.1007/s00348-012-1280-x.

[33] L. Zhou, D. Wang, B. Cao, and H. Xu, “Accurate Method for Estimating Wall-Friction Based on Analytical Wall-Law Model,” *Aerospace*, vol. 11, no. 7, p. 544, Jul. 2024, doi: 10.3390/aerospace11070544.

[34] L. A. Hendriksen, A. Sciacchitano, and F. Scarano, “3D particle tracking for skin friction and surface flow topology around generic objects,” Under revision.

[35] E. Rodríguez-López, P. J. K. Bruce, and O. R. H. Buxton, “A robust post-processing method to determine skin friction in turbulent boundary layers from the velocity profile,” *Exp. Fluids*, vol. 56, no. 4, p. 68, Apr. 2015, doi: 10.1007/s00348-015-1935-5.